

Western Kentucky University

TopSCHOLAR®

Masters Theses & Specialist Projects

Graduate School

7-2022

Evaluation Of Silver Nanoparticles Attached To Methylene Blue As An Antimicrobial Agent And Its Cytotoxicity

Somon Hakimov

Follow this and additional works at: <https://digitalcommons.wku.edu/theses>



Part of the [Biology Commons](#), [Chemistry Commons](#), and the [Physics Commons](#)

This Thesis is brought to you for free and open access by TopSCHOLAR®. It has been accepted for inclusion in Masters Theses & Specialist Projects by an authorized administrator of TopSCHOLAR®. For more information, please contact topscholar@wku.edu.

EVALUATION OF SILVER NANOPARTICLES ATTACHED TO METHYLENE BLUE AS
AN ANTIMICROBIAL AGENT AND ITS CYTOTOXICITY

A Thesis
Presented to
The Department of Physics and Astronomy
Western Kentucky University
Bowling Green, Kentucky

In Partial Fulfillment
Of the Requirements for the
Degree
Master of Science

By
Somon Hakimov

July 2022

EVALUATION OF SILVER NANOPARTICLES ATTACHED TO METHYLENE BLUE AS
AN ANTIMICROBIAL AGENT AND ITS CYTOTOXICITY

Date Recommended 07/07/2002

Dr. Ali Oguz Er, Director of Thesis

Dr. Simran Banga

Dr. Ivan Novikov

Ranjit T. Koodali

Associate Provost for Research and Graduate Education

I dedicate this to my family and teachers without whom I would not be here today; thank you for your endless support, particularly Erhan Guler, Parviz Hakimov, Ulugbek Mirzoev, Timur Ashurov, Fatih Gulek, Alexander Ismatov, Yusuf Balkas, Sabri Zerenturk, Ilhom Hotami.

ACKNOWLEDGEMENTS

I would like to thank immensely my advisor Dr. Ali Oguz Er for his expert advice, encouragement, and guidance throughout this challenging project, as well as Dr. Simran Banga for her help without whom the completion of this project could not have been accomplished. Also, I would also like to thank Ernek Belev, Salizhan Kylychbekov, Zikrulloh Khuzhakulov, Andrew Brooks, Jordyn Hurley, Shelby Emberton, Molly Bostic for their support and assistance in the lab. I am grateful to all of those with whom I have had the pleasure to work in the lab for their friendship and willingness to always help me.

This project would have been impossible without the support of Kentucky Biomedical Research Infrastructure Network (KBRIN). Finally, I would like to express my gratitude to Graduate School for supporting this project and providing the opportunity to present at many conferences.

TABLE OF CONTENTS

ABSTRACT	vii
Chapter 1. INTRODUCTION.....	1
1.1. Antibiotic resistance and photodynamic therapy.....	1
1.1. Silver nanoparticles (Ag NPs).....	3
1.2. Laser-matter interaction in liquid medium.....	4
Chapter 2. MATERIALS AND METHODS.....	10
2.1. Silver nanoparticles synthesis.....	10
2.2. Characterization of Ag NPs using electron microscopy.....	11
2.3. Characterization of Ag NPs using spectroscopy analysis	11
2.4. Photodynamic therapy experiment.....	12
2.5. Bacterial uptake measurement.....	13
2.6. Cytotoxicity assay.....	14
Chapter 3. RESULTS AND DISCUSSION.....	15
3.1. TEM measurements.....	15
3.2. UV-Vis spectroscopy.....	20
3.3. Photoluminescence measurements.....	23
3.4. Survival of <i>E. coli</i> and <i>S. aureus</i> in citrate, PVP, and PVA.....	24
3.5. Bacterial uptake.....	26
3.6. In Vivo cytotoxicity measurements.....	27
CONCLUSION.....	28
Appendix A: SAMPLE PREPARATIONS.....	30
Appendix B: Nd:YAG LASER OPERATIONS.....	42

References.....48

EVALUATION OF SILVER NANOPARTICLES ATTACHED TO METHYLENE BLUE AS AN ANTIMICROBIAL AGENT AND ITS CYTOTOXICITY

Somon Hakimov

July 2022

52 pages

Directed by: Ali Oguz Er, Simran Banga, and Ivan Novikov

Department of Physics and Astronomy

Western Kentucky University

Antibiotics resistance is considered as one of the greatest public health challenges of our time. In this work, we have synthesized silver nanoparticles (Ag NPs) using pulsed liquid ablation in different medium of growth and later combined with methylene blue (MB) to evaluate its potential as an effective photodynamic therapy agent. Ag NPs were synthesized by pulsed laser ablation technique in Polyvinylpyrrolidone (PVP), citrate, and Polyvinyl alcohol (PVA). The Ag NPs were characterized using transmission electron microscopy (TEM), UV-Visible (UV-Vis), and photoluminescence (PL) spectra. Next, Ag NPs were coupled with MB and used to deactivate the Gram-negative bacteria, *Escherichia coli* (*E. coli*), and Gram-positive bacteria, *Staphylococcus aureus* (*S. aureus*). MB and Ag NPs mixture exhibited a synergistic activity and was more effective compared to separate use of MB and Ag NPs. Ag NPs in PVP was shown to be the most effective media for bacterial deactivation. Given the concern for Ag NPs' cytotoxicity for adverse health effect, cytotoxicity measurement in HEK 293T cell lines were performed. Our results shows that Ag NPs do not exhibit significant cytotoxicity up to 50 µg/ml in each solution and MB/Ag NPs combination has potential to be used in PDT where standard photosensitizers have limitations.

CHAPTER 1

INTRODUCTION

1.1. Antibiotic resistance and photodynamic therapy

Antibiotics resistance is regarded as one of the greatest public health challenges of the modern time. The recently released report from Center for Disease Control and Prevention (CDC) estimates nearly three million antibiotic-resistant infections occur in the U.S. each year, and more than 35,000 people die as a result [1]. In addition, nearly 223,900 people in the United States required hospital care for *C. difficile* and at least 12,800 people died in 2017. Antibiotic resistant bacteria and fungi can spread across the globe through people, animals, and goods. Given increasing number of antibiotics and antiseptics resistant pathogens, there is a crucial need for antimicrobial approaches that are capable of inactivating pathogens efficiently without the risk of inducing resistance. Potential alternatives to antibiotics include using predatory bacteria, antimicrobial peptides, phages, gene editing enzymes, metals, and photodynamic therapy [2].

Among the possible methods to overcome this issue, photodynamic therapy (PDT) is a growing area of science, continually discovering new synthetic and natural photosensitizers (PS) for an efficient, cost-effective, and acceptable treatment for patients [3-5]. PDT is a treatment that uses photosensitizing agents which, when exposed to light, become toxic to targeted bacteria, malignant cells, and other diseased cells. PDT has become a frequently used alternative method for antibiotics and it is capable of eliminating antibiotic-resistant pathogens [4, 6, 7]. The treatment of bacterial infections by PDT has been successfully applied in dermatology [8-10] and oncological treatments [11], where phenothiazine dyes are applied to the infected skin area and then illuminated with red light [12].

Moreover, the way of destroying microbial pathogens in PDT has many advantages compared with the conventional antimicrobials and antibiotics used. It has a broad spectrum of action against bacteria, fungi, viruses, and protozoa [14]. In addition, its effect is almost immediate compared to days in conventional antibiotics as a result no development of resistant strains. In PDT, photosensitizer becomes excited upon exposure to light with a specific wavelength. Then the PS transfers its energy to molecular oxygen thus generating highly reactive singlet oxygen ($^1\text{O}_2$) as consequence damaging cell structure of microorganism and inducing death to targeted cell [13, 14].

As one of the key components of the PDT, an ideal photosensitizer must possess strong absorbance at long wavelengths, excellent photostability, lower dark toxicity, and high quantum yield of singlet oxygen ($^1\text{O}_2$) [15, 16]. One of such photosensitizers, Methylene blue (MB) is phenothiazinium dye with a strong absorbance in the range 550–700 nm and a quantum yield of 0.52 [17]. MB is frequently used against a bacterial infection for skin treatment, dental therapy, and showed promising results in *in vivo* regression of cancer and bacterial infections when irradiated by red light [9, 10, 18, 19].

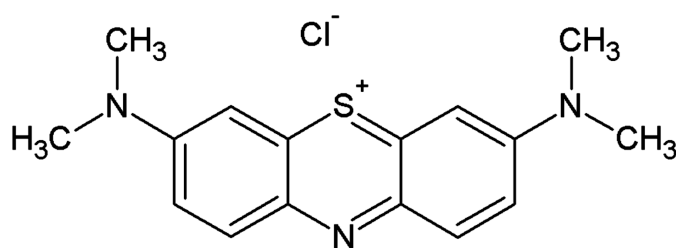


Figure 1 The molecular structure of methylene blue.

However, the photo-deactivation rate of MB was found to be significantly lower in plasma than in water, saline, and PBS solution due to cysteine attack into electron deficient central nitrogen in MB [20]. When MB is reduced, the value of the dipole moment of the excited states changes and MB does not absorb light to produce singlet oxygen. This process basically

makes MB ineffective bactericidal agent, especially in the human plasma [20]. To solve this problem and to improve MB as a more effective PDT agent, MB was attached to various carriers, including nanomaterials and quantum dots [13, 18, 21, 22].

Of these nanomaterials, silver nanoparticles (Ag NPs) are one of the most promising antimicrobial agent since they possess high germicidal activity against a broad range of microbes [23-25]. Moreover, the cost-effectiveness, availability as well as the lower toxicity towards human blood attracted considerable attention in infectious diseases treatments [26]. Disinfection with silver is well known wound management technique from ancient times [27]. The possible mechanisms and bactericidal activity of Ag NPs have been discussed extensively in literatures [28-30]. The major causes underlying the antibacterial effects of Ag NPs were explained as follows: (1) direct damage of bacterial cell membrane; (2) generation of reactive oxygen species by Ag NPs and silver ions; (3) penetration into the bacterial cell membrane; and 4) induction of intracellular antibacterial effects, including disruption of Adenosine triphosphate (ATP) production and DNA replication [28-30]. The most critical physical and chemical parameters that affect the antimicrobial potential of Ag NPs are size, shape, surface charge, concentration and colloidal state [31-33].

Ag NPs have been synthesized by many different methods to date [34]. Among these methods, pulsed laser ablation in liquid (PLAL) technique offers a fast, inexpensive, and environmentally friendly route to Ag NPs synthesis. In PLAL, various growth parameters such as composition of ablation liquid and laser parameters can be controlled easily [13, 14, 35]. The surfactants and volume-excluders were shown to affect the size and its distribution, and stability of nanoparticles. Also, the addition of a proper amount of NaCl reduced the particles size distribution [36]; the synthesized NPs' size was decreased with increased concentration of

sodium dodecyl sulfate (SDS); polyvinylpyrrolidone (PVP) aqueous solution improved colloid's stability as well as decreased the average size of NPs [37].

In this work, we synthesized Ag NPs in citrate, PVP, and PVA aqueous solutions, as well as in DI water using PLAL technique with different power and wavelength. NPs were then characterized by UV–vis spectroscopy and photoluminescence (PL) spectra. Average sizes and size distributions were measured by transmission electron microscopy (TEM). The synthesized Ag NPs in different aqueous solutions along with commercial Ag NPs were combined with MB to increase singlet oxygen generation and photo-responsivity. The results demonstrated that MB/Ag NPs mixture was more effective antibacterial compared to MB or Ag NPs alone. The MB/Ag combination eliminated all Gram–negative and –positive bacteria colonies at different time intervals for different mediums. In addition, the cytotoxicity and bacterial uptake were measured. Ag NPs were not toxic up to 50 µg/ml concentrations. Our results show that MB/Ag NPs combination can potentially be an effective tool to deactivate different strains of pathogens in open wounds without exhibiting any cellular cytotoxicity.

1.2. Laser-matter interaction in liquid medium.

To understand the growth of Ag NPs by PLAL, we need to look at the mechanism of growth. Laser-matter interaction of a solid target in atmosphere or vacuum contains physical processes however, solid target in liquid medium contains physical processes and chemical processes as well [38].

Laser pulse duration, repetition of the pulse, wavelength, and intensity of the laser beam are important factors to consider in laser material interactions [39, 40]. Properties of a target such as optical absorption, mechanical, and thermal features also play important role in laser-matter interaction [38].

Lasers with pulse width of nanosecond, picosecond, and femtosecond has a different impact on melting, ablation, and plasma plume formation [39-42]. To ablate the material, energy of the individual photon should exceed the energy of binding atoms, resulting dependency of ablation on the fluence of laser [39].

When a laser beam interacts with matter, photons are absorbed by electrons and become excited, and some electrons gain excessive energy and leave the target ionizing it. Then, electrons transfer their energy to inner lattice by means of electron-phonon (electron-ion collisions), that takes time called temperature equilibrium-time, t_e , also known as electron cooling time. Energy transfer time of electrons to lattice is called heat conduction with characteristic time t_i , also known as lattice heating time [39].

The energy transfer from the laser beam to the target material can be described using one-dimensional, two-temperature diffusional models when this is considered rapid thermalization in the electron subsystem. In this case, lattice and electron subsystems are characterized by their temperatures (T_i lattice temperature and T_e electron temperature) separately. Equation below shows how energy transfer takes place [40, 42].

$$C_e \frac{\partial T_e}{\partial t} = -\frac{\partial Q(z)}{\partial z} - \gamma(T_e - T_i) + S \quad (1)$$

Equation (1) shows the energy balance for the metal absorbing the laser beam and how the temperature of electrons changes as a function of time.

$$C_i \frac{\partial T_i}{\partial t} = \gamma(T_e - T_i) \quad (2)$$

Equation (2) shows energy that is absorbed by lattice as a function of time.

$$\partial Q(z) = -k_e \left(\frac{\partial T_e}{\partial z} \right) \quad (3)$$

Equation (3) describes the absorbed energy as a heat in the skin layer along the z -axis perpendicular to the target material surface.

$$S = I(t)A\alpha e^{-\alpha z} \quad (4)$$

Equation (4) shows the initial energy that is coming from a laser and being absorbed as the function of time.

$Q(z)$ is the absorbed heat flux in the skin layer along the z -axis perpendicular to the target material surface, S is the laser heating source, $I(t)$ is the laser intensity (W/cm^2) as a function of time, A is the surface transmissivity ($A = 1 - R$), R is the reflectivity of the target material, α is the absorption coefficient of the target material, C_e is the heat capacity of the electrons per unit volume, C_i is the lattice heat capacity per unit volume, γ is the parameter characterizing the electron-lattice coupling, k_e is the thermal conductivity of the electrons or the heat transfer coefficient between the electrons and the lattice is independent of temperature.

Two non-linear differential equations (1) and (2) are used to model the cooling dynamics for T_e and T_i , which account for the electron-phonon coupling and thermal conductivity of the sample material [43]. In addition, these equations can be used to model the time evolution of the electron and lattice temperatures, T_e and T_i [40]. Equations (2), (3), and (4) can be inserted into equation (1) then equation (5) is derived

$$C_e \frac{\partial T_e}{\partial t} = k_e \left(\frac{\partial^2 T_e}{\partial z^2} \right) - C_i \frac{\partial T_i}{\partial t} + I(t)A\alpha e^{-\alpha z} \quad (5)$$

In Eq. (5), a thermal conductivity in the lattice subsystem (phonon component) is neglected. Eq. (5) has three characteristic timescales, t_e , is electron cooling time, t_i is the lattice heating time ($t_i \gg t_e$ because heat capacity of the lattice, C_i , is much greater than heat capacity of electrons,

C_e), and t_L is the laser pulse duration time. These three parameters explain three different types of laser-matter interaction: nanosecond, picosecond, and femtosecond [40, 42].

In picosecond ablation, free electrons will absorb most energy therefore temperature increases fast due to Bremsstrahlung. However, it loses some of its energy in around 10 picoseconds and cools down [40]. Lattice heating time is much longer than electron losing energy time or electron-phonon energy transfer time $t_i \gg t_e$. In this situation, temperature of the lattice is relatively lower than the temperature of electrons and the lattice temperature does not change much. Hence, this condition $t_i \gg t_L \gg t_e$ is fulfilled. When pulse width is shorter than heating lattice time, the temperature of electrons becomes higher than the temperature of lattice as explained above, this is also known as a non-thermal equilibrium state [40]. When $t_e \ll t_L$, both initial lattice temperature and final lattice temperature are approximately equal [39].

In femtosecond laser, pulse width is much shorter than electron cooling time $t_L \ll t_e$, hence ablation occurs before electrons transfer their energy to lattice. With picosecond and femtosecond lasers, solid directly transforms to vapor and plasma plume, melting and heat affected zone observed in nanosecond laser and not observed in ultrafast ablation [39, 45]. For instance, in Cu metal ablation, the time for the transfer of energy from electrons to ions by electron-phonon collision, t_e , is $7 \cdot 10^{-12}$ s and for Si is $6.4 \cdot 10^{-12}$ s. Time for transfer of heat from electrons to lattice by electron heat conduction, t_i , in Cu is $45 \cdot 10^{-12}$ s. These values show that the ions (lattice) remain cold if laser beam has pulse width of picosecond or shorter time. Hence, all the absorbed energy is confined in the electron component and energy spread will be negligible [39].

In nanosecond laser ablations, electrons transfer their energy to lattice in about 10^{-10} - 10^{-12} second for metals [39-42, 44], hence in metals with nanosecond pulse duration, electrons have

enough time to relax and transfer their energy to lattice. The pulse duration time is too long in this situation $t_L \gg t_i \gg t_e$, therefore thermal equilibrium establishes between temperature of electrons, and lattice. Ablation is considered thermal; therefore, the matter first heats up to melt then evaporates. Hence, creating heat affected zone (HAZ), melting, and other undesired effects. With nanosecond laser producing thin films with high qualities is difficult and it is generally used for ejecting materials [40, 42, 44].

Nanosecond-pulsed laser ablation in liquid (ns-PLAL) includes generation, transformation, and condensation of plasma plumes [46]. Initially plasma is generated by laser ablation of a solid target at the interface when the laser ablates the target immersed in a liquid. The plasma plume mainly results from the multiphoton absorption, ionization, and inverse Bremsstrahlung in the gaseous phase induced by laser ablation. The plasma plume contains atoms, molecules, ions, and electrons from the solid. This initial plasma is called laser-induced plasma Fig. 2a [47]. Then, unlike in vacuum and gas environments, the expansion of the laser-induced plasma is confined by the liquid. After the solid target absorbs the later part of the laser pulse to produce a continual supply of vaporizing species, the plasma adiabatically expands to

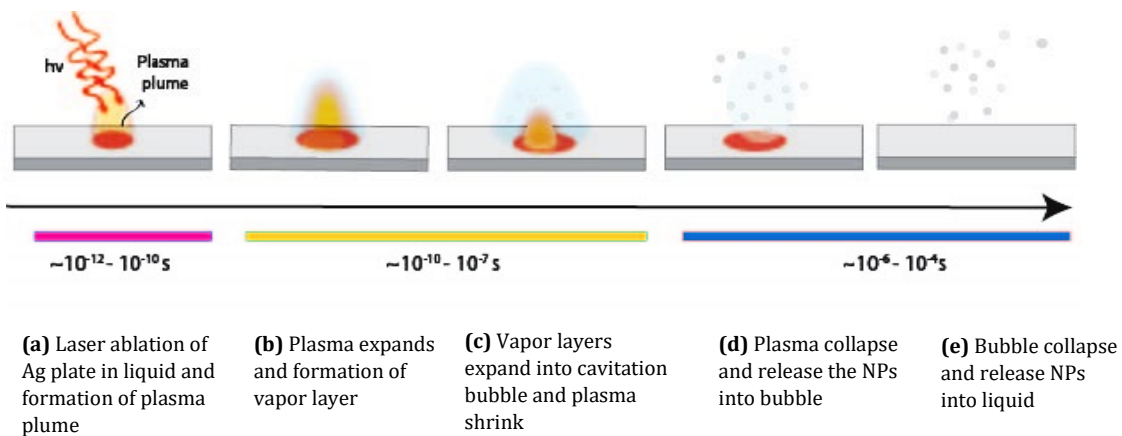


Figure 2 Mechanism of laser interacting with solid silver plate and generating Ag NPs.

create a shock wave, which results in extra pressure and temperature in the plasma Fig. 2b [47].

During the expansion and condensation of the plasma plume, it transfers energy to the surrounding liquid, which causes a thin layer of vapor to rise. This vapor layer is the early stage of cavitation bubbles. The last stage of development of a plasma plume in a liquid is cooling and shrinking accompanied with decreases in pressure and temperature because of the confinement of the liquid Fig. 2c. Finally, the plasma quenches and releases small nanoparticles Fig. 2d. A time sequence of this evolution process is shown in Fig. 2 [47]. When the vapor layer is generated, it starts to expand and compresses the plasma back against the target more efficiently than the surrounding liquid Fig. 2c. In general, expansion and shrinkage are dynamics of cavitation bubbles. The lifetime of bubble is not the fixed value, which depends strongly on laser pulse characteristics, such as laser fluence [48]. The bubble size is closely related to the pulse width, which indicates that the longer the laser pulse is, the larger the bubble will be in the bubble expansion process. The final collapse of the bubble released its interior mass into the liquid, including clusters and nanoparticles Fig. 2e. The produced clusters and nanoparticles are unstable initially, and probably tend to agglomerate. Surfactant can be used in this regard to avoid aggregation [38].

As mentioned above, the bubble originates from the thin layer of vapor around the plasma plume. The vapor reaches a high temperature because the plasma transfers energy to it. Like plasma, the vapor layer starts to expand to transform into a bubble with larger radius than that of the vapor layer. The confinement of the liquid increases the pressure inside the bubble. After the plasma expands and transfers its energy to the vapor layer, it gradually cools down [47]. Therefore, the bubble expands in all directions, not only moving against the liquid, but also moving against and compressing the plasma [49].

CHAPTER 2

MATERIALS AND METHODS

2.1. Silver nanoparticles synthesis

Ag NPs were synthesized in four different aqueous solutions including Deionized water (DI), Polyvinylpyrrolidone (PVP), Polyvinyl alcohol (PVA), and sodium citrate. Stabilizers such as citrate, PVP, PVA, and other organic molecules, peptides, polymers are often used to prevent particle aggregation [50]. The PVP, PVA, and silver plate were supplied from Sigma-Aldrich and the Sodium Citrate was purchased from Fisher Scientific. The average molecular weight of PVP was 10,000 and for PVA 9500 g/mol with 80% of acetate being hydrolyzed. The Ag NPs were synthesized by targeting the silver plate using a Nd: YAG laser beam (Continuum Surelite II, 10 Hz repetition rate, and 5 ns pulse duration) at 1064 and 532 nm wavelength. The silver target (99.99%, thickness 1.0 mm, width and length 1 × 1 inch) was attached to the top of a small aluminum table using double-sided carbon tape. The aluminum table with silver target and a magnetic stirring bar were inserted into a 50 ml beaker, then 24 ml of designated aqueous solution was added to the beaker, to make the height of the solution above the target 11 mm. Next 50 mL beaker was placed on the magnetic stir plate, stirring continuously during the synthesis to prevent accumulation of Ag NPs above the target and to minimize shielding effects. The XY-translational stage was placed under the magnetic stir plate and was moved in XY directions continuously to get uniform ablation of the target as shown in Fig. 3. The laser was used at three different energies, 50, 100, and 200 mJ/pulse for each wavelength, 1064 and 532 nm. The purpose of using different energies was to see if the size of Ag NPs would change. A converging lens of 30 cm focal length was used to focus the laser beam on to the target. The height from the target to lens was 23 cm in order to make spot size of the laser beam 1 mm, after

focusing. The ablation time was 10 min for each synthesis, except 25 min for PVA. The PVA required more time probably due to a different rate of plasma confinement and hence lower plasma temperature and lower rate of synthesis compared to citrate and PVP.

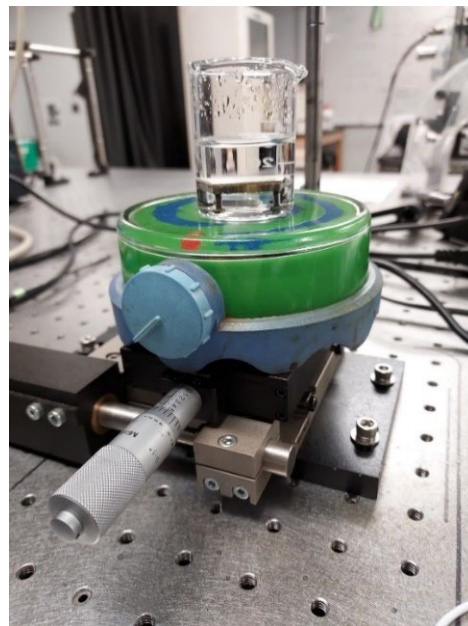
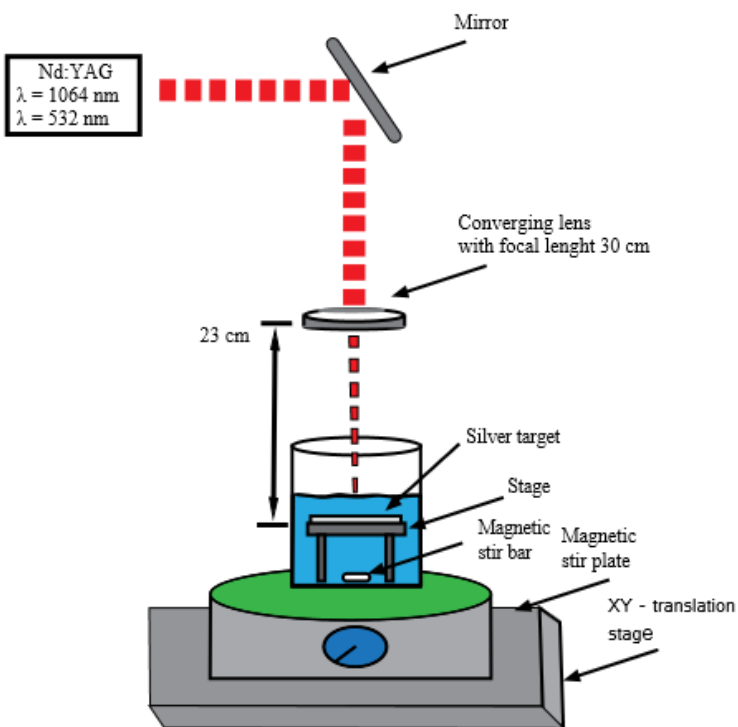


Figure 3 The design of experimental set up that was used to synthesize Ag NPs.

2.2. Characterization of Ag NPs using electron microscopy

After synthesis of Ag NPs, the characteristics such as shape, average size, and size distribution were determined through TEM (JEOL JEM- 1400 plus) images by placing a droplet onto a 300-mesh copper TEM grid.

2.3. Characterization of Ag NPs using spectroscopy analysis

UV-vis spectrophotometry was used to measure the absorbance of the Ag NPs in different solutions to confirm presence of Ag NPs and measure their concentrations.

Photoluminescence was used to determine photophysical properties of Ag NPs, such as luminescence, for NPs synthesized in all three mediums, PVP, PVA, and Citrate.

2.4. Photodynamic therapy experiment

The antibacterial activity of Ag NPs, MB, and MB/Ag NPs mixture were assessed using gram-positive *S. aureus* and gram-negative *E. coli* bacteria. Bacteria were cultured in LB broth medium for 18-24 hours and a bacterial suspension was prepared to 10^8 CFU/ml using spectrophotometer. A total of 8 different sample groups were prepared (1) bacteria only, (2) bacteria + Ag:Cit, (3) bacteria + Ag:PVP, (4) bacteria + Ag: PVA, (5) bacteria + MB (6) bacteria + MB + Ag:Cit (7) bacteria + MB + Ag:PVP, (8) bacteria + MB + Ag:PVA. After preparing these combinations using 2 separate 6-well plates, from each plate only four wells were used, next plates were covered with aluminum foil and the samples were mixed in the absence of light for 10 min. All combination of samples is put in Fig. 4. Next, each sample was exposed to red LED light for 1–15 min Fig. 5. Following, each sample was serially diluted, plated and incubated for 24–48 hours at 37 °C. The experiment was repeated 4, 5 times and GraphPad Prism v6 was used to perform statistical analysis and represent the data.

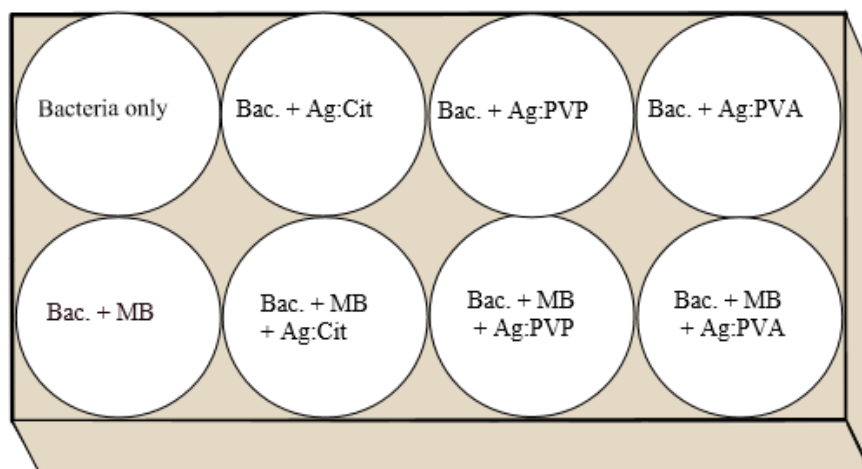


Figure 4 All combination of solution samples are listed in the well plates that were used in the experiment.

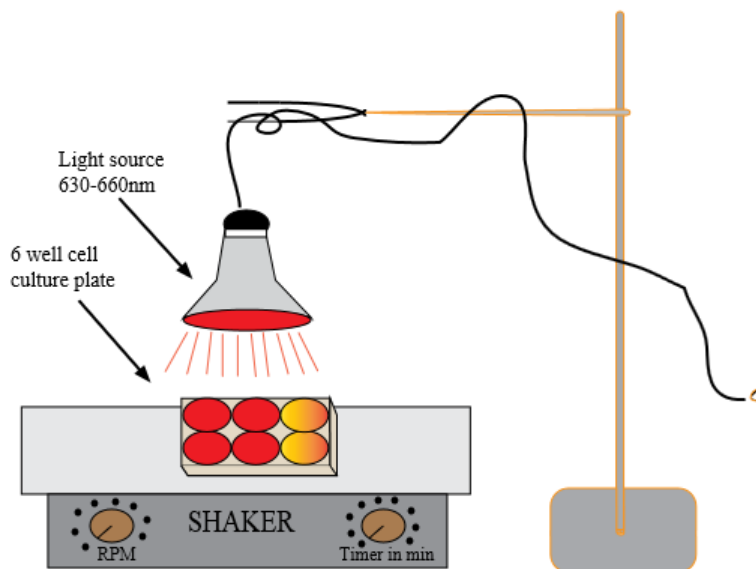


Figure 5 The design of the set up that was used for PDT experiments. Out of 6 – well plates only 4 were used at once since light was not fully reaching two other well plates.

2.5. Bacterial uptake measurement

Samples were placed in tip of a mold containing epon araldite resin and allowed to dry in order to create a block. Blocks of samples were then trimmed with a razor blade until a 1 mm by 1mm trapezoid of sample rich block face was created which was then smoothed to an even surface using a diamond tipped milling machine. The blocks of sample were then placed in an ultra-microtome, in which a glass knife was used to cut 85-90 nm thick sections of sample. A Copper TEM grid for each sample was cleaned with HCl, and briefly submerged in water and acetone. These grids were then used to attach 4–8 sections of samples and then submerged in one percent uranyl acetate for twenty minutes. Grids were then submerged in 25 ml of sterile, distilled water for ten seconds to wash off the uranyl acetate. This was repeated three times with fresh sterile, distilled water. Grids were placed in lead citrate with 20 mM NaOH for three minutes. Finally sample grids were rinsed for 10 s in three containers containing 25 ml of

recently boiled water starting with the container containing 100 μ L NaOH. Samples were then viewed with TEM to get images.

2.6. Cytotoxicity assay

HEK 293T Cell lines obtained from the American Type Culture Collection was grown in DMEM medium with 10% FBS. The MTT 3-(4,5- dimethylthiazol-2-yl)-2,5-diphenyltetrazolium bromide cellular viability assay was performed by seeding 10,000 cells per well in 96-well plates that were incubated at 37 $^{\circ}$ C in 5% CO₂. After 24 h, the wells were treated in replicates to different concentrations of silver nanoparticles ranging from 1 to 50 microgram/ml synthesized in citrate, PVP and PVA for 24 h. A negative control (media only), positive control (0.1% Triton X-100) and series of blanks containing treated and untreated cells were simultaneously established. The assay was carried using MTT assay kit from Sigma-Aldrich as per manufacturer's instructions. Briefly, the assay was run for 5 h, then the wells were treated with solubilization solution overnight before the plates were read using a BioTek Synergy HT microplate reader (570 nm and 690 nm). GraphPad Prism v6 was used to perform statistical analysis and represent the data.

CHAPTER 3

RESULTS AND DISCUSSIONS

We have used samples synthesized in different medium with pulsed laser synthesis method as described above. Different characterization methods have been used to evaluate the morphology, physical, and chemical properties of the Ag NPs.

3.1. TEM measurements

Nanoparticles exhibit unique properties due to their high surface area to volume ratio and quantum confinement when their particles sizes are near or below their exciting Bohr radius. To find the shape, average size and size distribution of Ag NPs, transmission electron microscopy (TEM) was used.

Fig. 6 shows the TEM images of Ag NPs in 2 mM citrate, PVP, PVA, and DI water. It was observed that NPs have a spherical shape, especially those synthesized in citrate, PVP and DI water. In the PVA, some NPs had elliptical (egg-shape) and rod shapes while majority being spherical, also some of them were aggregated (Fig. 6 e and f). It is known that NPs tend to be very reactive since their surfaces possess a high density of dangling bonds and defects when they are synthesized. Due to the small grain sizes and the high surface energy, assembling of nanoparticles to reduce the surface energy can become a prominent process [51]. The primary attractive force is Van der Waals (VDW) for the stabilization of nanoparticles when they aggregate. This force is proportional to particle size and has a power law dependence (inversely proportional to the square of particle separation) on interparticle distance and extends to longer distance. It should be noted that there are other forces such as electric, hydration, hydrophobic, and electronics forces that influences the stability of the NPs in liquid medium.

NPs were aggregated in DI water while there were no signs of aggregation in citrate and

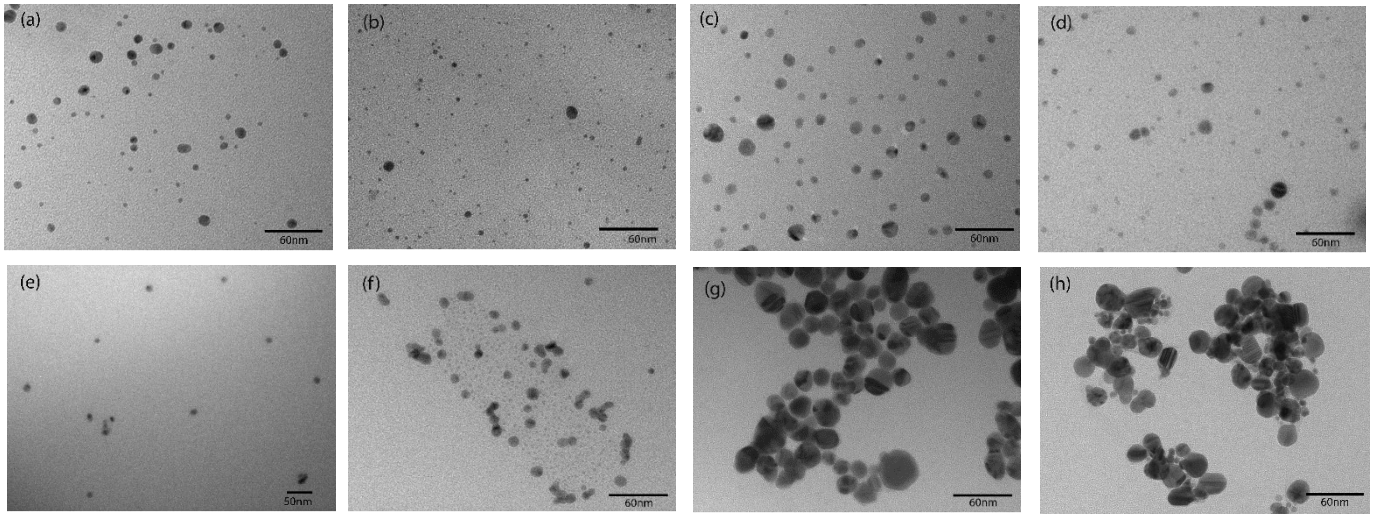


Figure 6 Ag NPs in a citrate medium, 1064 (a) and 532nm (b); PVP medium 1064(c) and 532 nm (d), PVA medium 1064 (e) and 532 nm (f), DI water 1064 (g) and 532 nm (h) with 200 mJ/pulse (2W power) energy.

PVP. Various parameters such as power, liquid height, spot size of laser beam, and irradiation time were altered in attempt to prevent aggregation in DI water, however, aggregation was still observed. Ag NPs in DI water were aggregated when they were synthesized using PLA technique due to adhesive force being larger than repulsive force [52-56]. Due to the high surface area to volume ratio which provides higher surface energy, Ag NPs tend to aggregate during or after the ablation to minimize the surface energy [51, 52, 57]. NPs in their surface have large number of atoms that have unsaturated coordination (unformed bonds) known as dangling bonds, which makes bonds upon interaction with adjacent NPs resulting in aggregation [57]. The attachment may also involve metallic bonds and Van der Waals forces [51]. Ag NPs were grown in different media, wavelength, and laser energy densities. Fig. 7 shows Ag NPs in citrate

medium with 1064 and 532 nm at 50, 100, and 200 mJ/pulse laser energies. Our statistical analysis shows that laser fluence at each wavelength does not affect the NPs' mean size. For example, in citrate medium with 1064 nm using 50, 100, and 200 mJ/pulse laser energies,

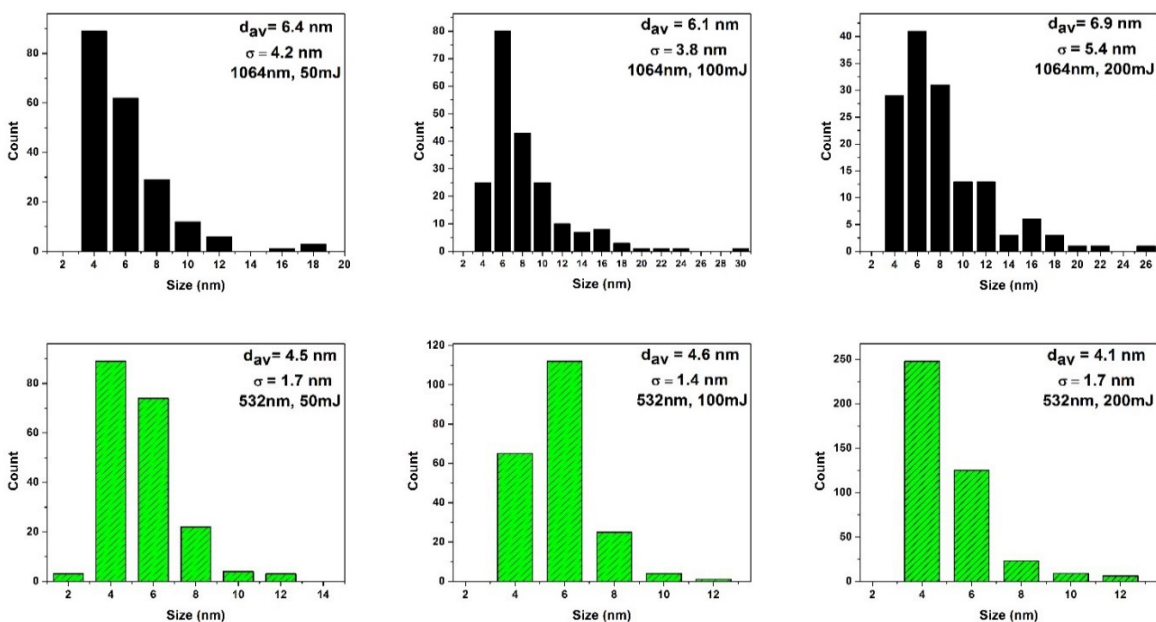


Figure 7 Size distribution of Ag NPs in a citrate solution, using 1064 nm and 532 nm wavelength, and 50, 100, 200 mJ/pulse laser energy respectively.

resulted in 6.4, 6.1, and 6.9 nm average size respectively, averaging around 6.5 nm. Similarly, in citrate with 532 nm laser, using three laser energies the average sizes were found to be 4.5, 4.6, 4.1 nm respectively, averaging in 4.4 nm. A similar pattern was observed for Ag NPs in PVP and PVA media as shown in Figs. 8 and 9. For instance, Ag NPs in PVP and PVA media using 1064 nm laser (upper panels) for all three energies averaged in 10.2 and 12.6 nm, respectively. The 532 nm laser pulses (lower panels) with three different energies resulted in average size of 7.4 and 10.0 nm, respectively.

Laser fluence is expected to play important role in determining the average size and its effect depending on the sample [58]. For instance, increasing the laser energy caused a decrease in Au nanoparticles and Cu nanoparticles sizes in acetone [59], and increase in ZnO nanoparticle

sizes with more spherical, homogeneous and broad size distribution [58]. The change in the particle size with laser energy is mainly due to pressure of the liquid vapor. In our case, the pressure generated by laser energy may not be enough to saturate either the vapor pressure or it may be low enough, so droplets go back to laser plasma. Therefore, size may not be affected within the certain range.

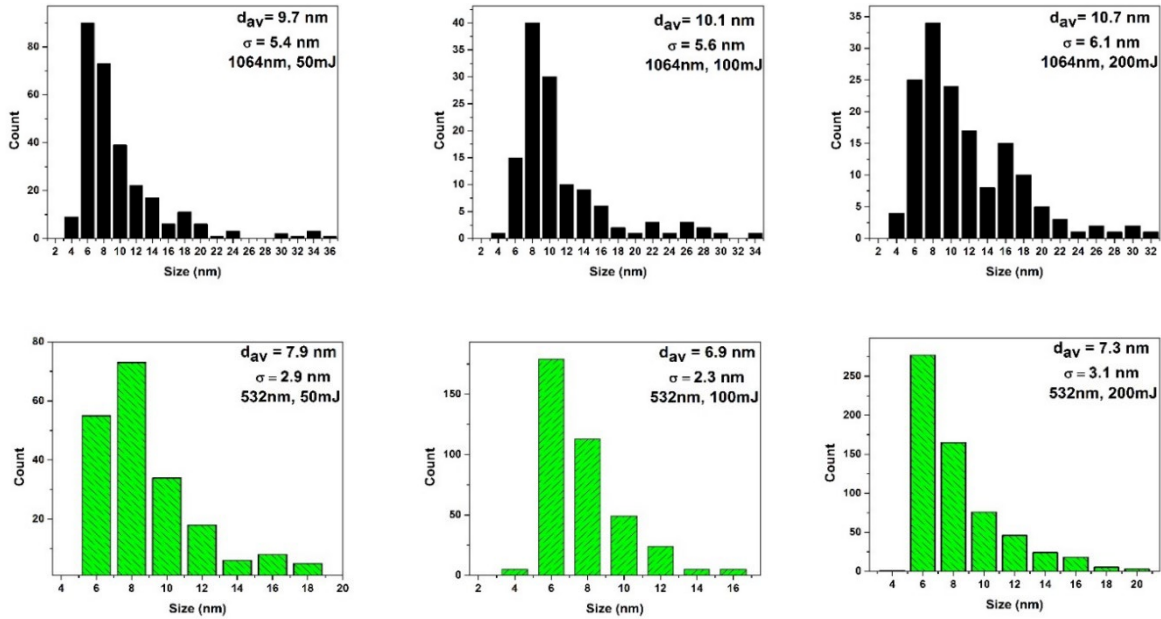


Figure 8 Size distribution of Ag NPs in a PVP solution, using 1064 nm and 532 nm wavelength, and 50, 100, 200 mJ/pulse laser energy respectively.

When 532 nm is used to obtain Ag NPs, the average size of the NPs decreased. As seen in Fig.7, 1064 nm laser pulses in citrate creates more irregular size of Ag NPs with larger standard deviation, 6.9 ± 5.4 nm. On the other hand, citrate at 532 nm creates NPs with a more uniform size and smaller average size, 4.1 ± 1.7 nm. The same pattern was observed in Ag NPs synthesized in PVP and PVA media, as shown in Figs. 8 and 9. For instance, using 1064 nm and 200 mJ/pulse laser energy, we observed average size to be 10.7 ± 6.1 nm and 12.2 ± 9.1 nm for PVP and PVA media, respectively. When 532 nm with 200 mJ/pulse laser energy is used, we

observed more uniform nanoparticles with average size of 7.3 ± 3.1 nm and 10.3 ± 2.4 nm for PVP and PVA media, respectively.

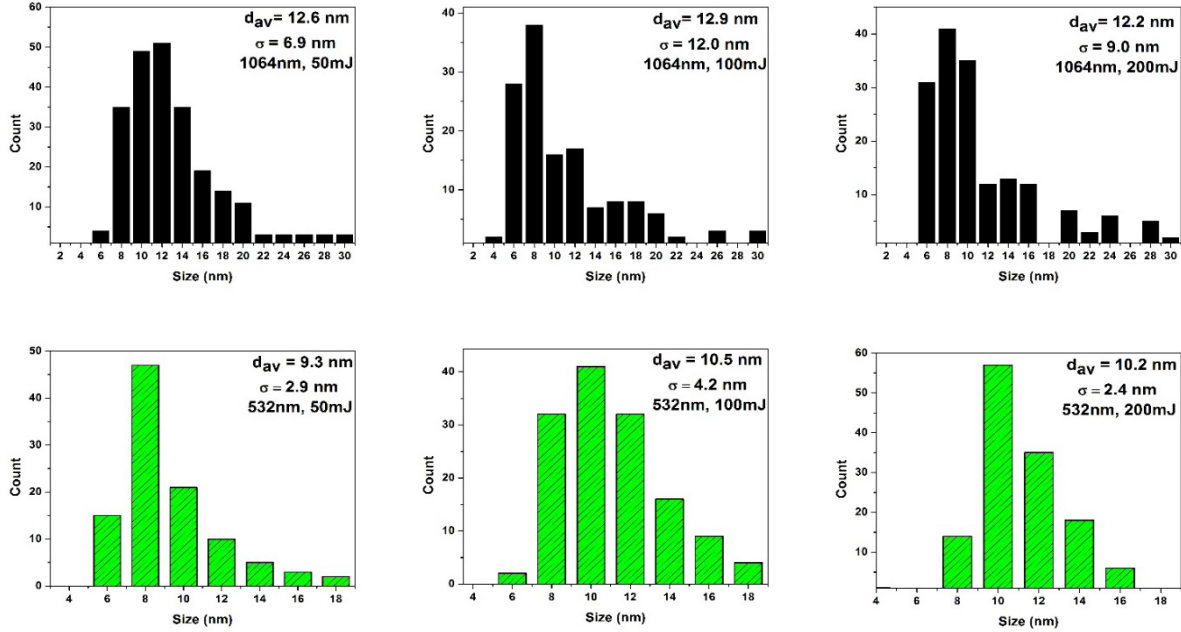


Figure 9 Size distribution of Ag NPs in a PVA solution, using 1064 nm and 532 nm wavelength, and 50, 100, 200 mJ/pulse laser energy respectively.

In addition, the color of Ag NPs synthesized with 1064 nm was brown, however with 532 nm the color was bright yellow due to different size and concentration of Ag NPs. In all mediums, the change of laser energy with the same wavelength did not bring a significant change in their size distributions. However, the concentration of the nanoparticles reduced with a decrease in laser energy. A change in size distribution was also observed when the wavelength and growth medium were changed.

The rate of nucleation and growth for silver nanoparticles for each medium is expected to be different due to different refractive index values. The ablation efficiency also increases with decreasing laser wavelength because of the increasing photon energy, and this is related to the size decrease of the as-prepared nanoparticle [60]. This can be ascribed to the fact that absorption

coefficient is inversely proportional to the wavelength. It was observed that the concentration of Ag NPs synthesized in PVA were lower compared to PVP and citrate medium. Thus, to achieve the same concentration of nanoparticles as synthesized in PVP and Citrate, the PVA was ablated for 25 min.

In addition, the concentration of Ag NPs with 1064 nm was much higher in TEM images, therefore it was diluted 5-fold then images were taken for measurements.

3.2. UV-Vis spectroscopy

UV-VIS spectroscopy is used as a characterization technique that can provide information about the size and shape of silver particles. Solutions of transition metal ions can be colored (i.e., absorb visible light) because d electrons within the metal atoms can be excited from one electronic state to another.

The absorption around 400 nm is typical plasmon absorption of Ag NPs when the frequency of the incident photon is resonant with the collective electron oscillations on the surface of the Ag NPs [61]. These vibrations are dependent on size, shape, dielectric medium,

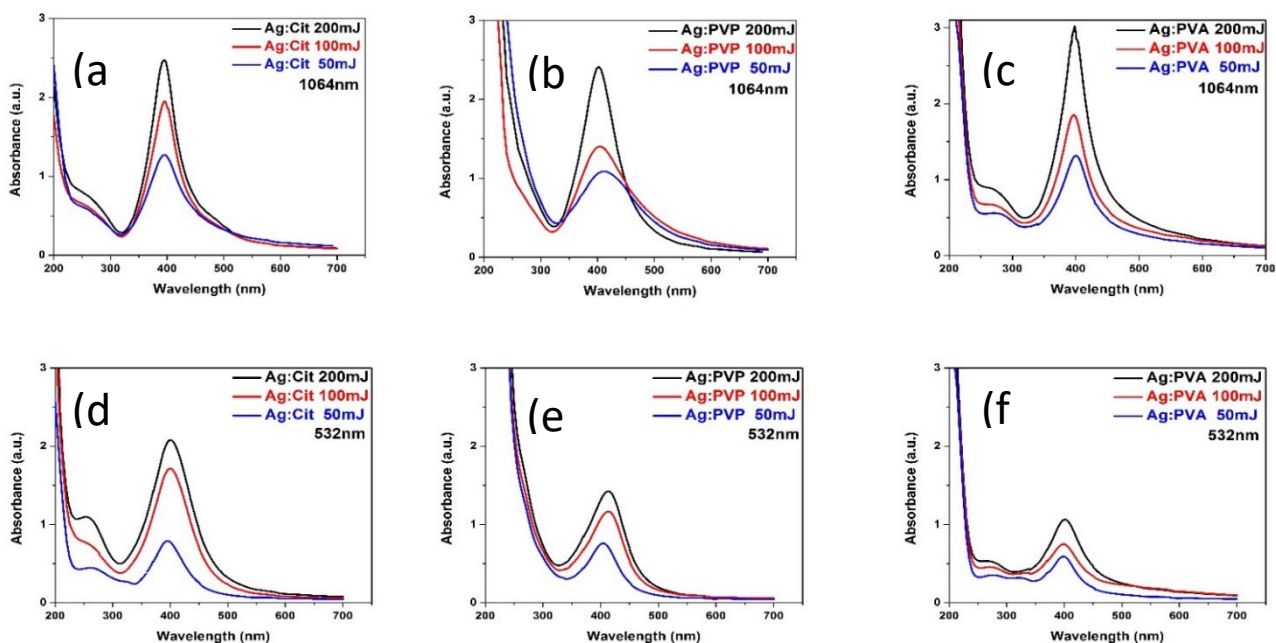


Figure 10 UV-Vis spectra of (a) citrate, (b) PVP, and (c) PVA with 1064 nm and 532 nm.

and chemical surroundings of the nanoparticles [62]. The intensity of the plasmon band increases with increasing laser fluency, whereas its position does not vary significantly.

The small spherical nanocrystals are expected to exhibit a single surface plasmon band, whereas anisotropic particles should exhibit two or three bands, depending on their shape according to the Mie's theory [63]. The larger metal colloidal dispersions can exhibit broad or additional absorption bands in the UV-Vis range due to the excitation of plasma resonances or quadrupole and higher multipole plasmon excitation [62]. In Fig. 10 a higher absorbance of Ag NPs band is observed at 200 mJ/pulse while absorbance has become lower for 100 mJ/pulse laser energy. Our results show that absorption of the Ag NPs increases with laser fluency, indicating the higher concentration of the sample. The UV-VIS measurement supports the TEM observations where similar trend in absorbance is observed with the laser power.

The peak absorbance in UV-Vis was between 395 and 404 nm. For example, for Ag NPs synthesized using 1064nm laser wavelength in citrate, PVP, and PVA media the peak of absorbance was 395, 395, and 400 nm, respectively; using 532 nm wavelength: 395, 404, and 400 nm, respectively. There was no change of peak absorbance for citrate and PVA, however a slight change is observed in PVP medium. The difference in sizes of nanoparticles grown in same medium with different wavelength is between 2 and 3 nm therefore no significant changes in the peak absorbance was observed. The effect of solvents on Ag NPs size distribution have been studied previously [64, 65]. It was shown that the smaller particle sizes were obtained in propanol, while the larger ones were obtained in ethanol [64]. The optical properties of the synthesized Ag NPs were strongly dependent on the solvent used [65]. The observed size difference and stability of suspensions were attributed to combination of viscosity and solvent's dipole moment. The absorption peaks shifted red when ablation wavelength of 532 nm is used

instead of 1064 nm. Usually, the peak absorbance wavelength increases with particle diameter, and for uneven shaped particles such as gold nano-urchins, the absorbance spectrum shifts significantly into the far-red region of the spectrum when compared to a spherical particle of the same diameter [66, 67]. Given that our diameter of the nanoparticles at 1064 and 532 nm, the shapes of the nanoparticles is believed to play an important role for red shift.

The formation of silver nanoparticles under laser irradiation of metallic silver is due to a strong interaction of the evaporated metal with liquid medium. When Ag absorbs the initial part of the laser beam, a thin layer of Ag is heated above its melting temperature during laser pulse. Ag transfers its heat to the adjacent water layer to almost the same temperature. One can estimate the thickness of this liquid layer by taking into account the heat diffusion coefficient of liquid water ($2.1 \times 10^3 \text{ cm}^2/\text{s}$ at 22°C) and diffusion time equal to the duration of the laser pulse (10 ns). Therefore, the thickness of the liquid layer is estimated around 0.1 micrometer with temperature reaching much higher values than boiling point at normal pressure. In our case, this thickness should be smaller than 0.1 micrometer owing to lower values of the PVA, PVP and citrate compared to the water. As the temperature of liquid increases, its vapor pressure also increases. When a solid or a liquid evaporates to a gas in a closed container, the molecules cannot escape. The high vapor density induces high molecular collisions per second and some of the gas molecules will eventually strike the condensed phase and condense back into it.

It is known that the rate of ablation and particle generation depend on the refractive index, the layer width of the liquid media, and laser ablation wavelength [68]. The refractive index is known to be a complex variable with real and imaginary parts. Both real and imaginary parts of the refractive index depend on the wavelength and their relationship can be described by Kramers-Krönig relationships. While real part is responsible for scattering, the imaginary part is

responsible for absorption. Usually, the lower the refractive index, the less absorption and lower rate of ablation.

3.3. Photoluminescence measurements

Photoluminescence (PL) emission spectroscopy was used as a method to further characterize the Ag NPs optical properties. As shown in Fig. 11, PL was measured for the Ag NPs in solutions of citrate, PVP, and PVA. Ag NPs emit visible light at different wavelengths depending on excitation wavelength. Changes in optical spectrum are dependent on the size, spatial orientation, shape, and optical properties of both the nanoparticles themselves and the solvent medium [69]. Synthesis medium of the Ag NPs has a notable impact on the PL spectra

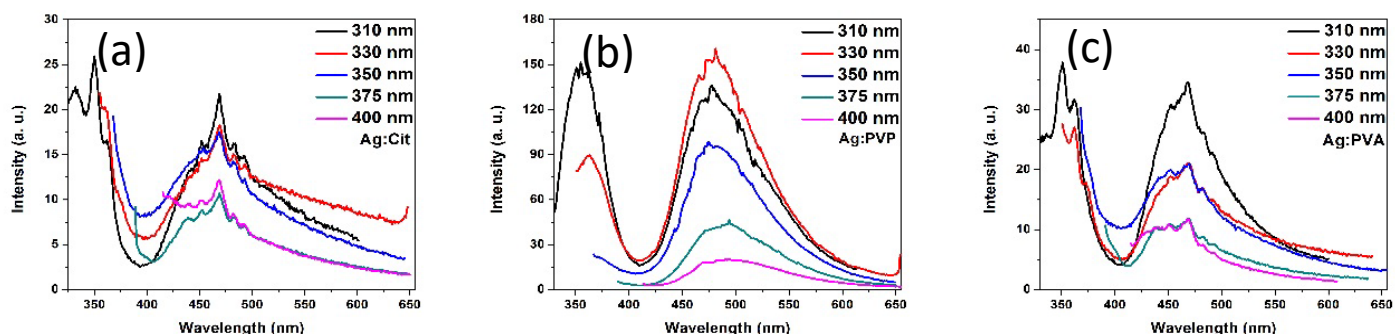


Figure 11 6 nm Ag NPs in citrate (b) 10 nm in PVP and (c) 12 nm in PVA.

shape. The intensity of emission increases dramatically as the particle size increases due to surface plasmon resonance (SPR) in the same medium as we previously showed [14, 70]. SPR is a series of coherent oscillations that lead to an enhanced local electric field near the surface of the particles [70, 71].

Our results show that the Ag NPs exhibits a wavelength- and medium-dependent emission spectra. A similar pattern is observed in all three solutions in which lower wavelengths of excitation emitted a higher intensity with a notable exception in presence of PVP wherein the intensity peaks for 480–500 nm emission shows the 330 nm excitation receiving an emission

notably larger than that of 310 nm. A significant difference was seen in intensity between the three media, with PVP having a much higher peak.

3.4. Survival of *E. coli* and *S. aureus* in citrate, PVP, and PVA

We studied the bacterial deactivation rate in different medium for two different strains of bacteria. Fig. 12 shows that bacterial colony forming units (CFU) remain same for both strains in PBS, used as a control, regardless of irradiation time. Also, when both strains were treated with Ag NPs alone in three different media no reduction of bacteria was observed. When *S. aureus* with MB is irradiated, number of colonies decreased from 10^8 to 10^3 in 8 min and for *E. coli* with MB it reduced from 10^8 to 10^4 CFU/ml. However, when MB and Ag NPs are used together, the same reduction rate is achieved within a shorter time for both strains. For instance, MB/Ag NPs deactivated 10^8 CFU/ml of *E. coli* completely in 6 min in citrate, 3 min in PVP, and 8 min in

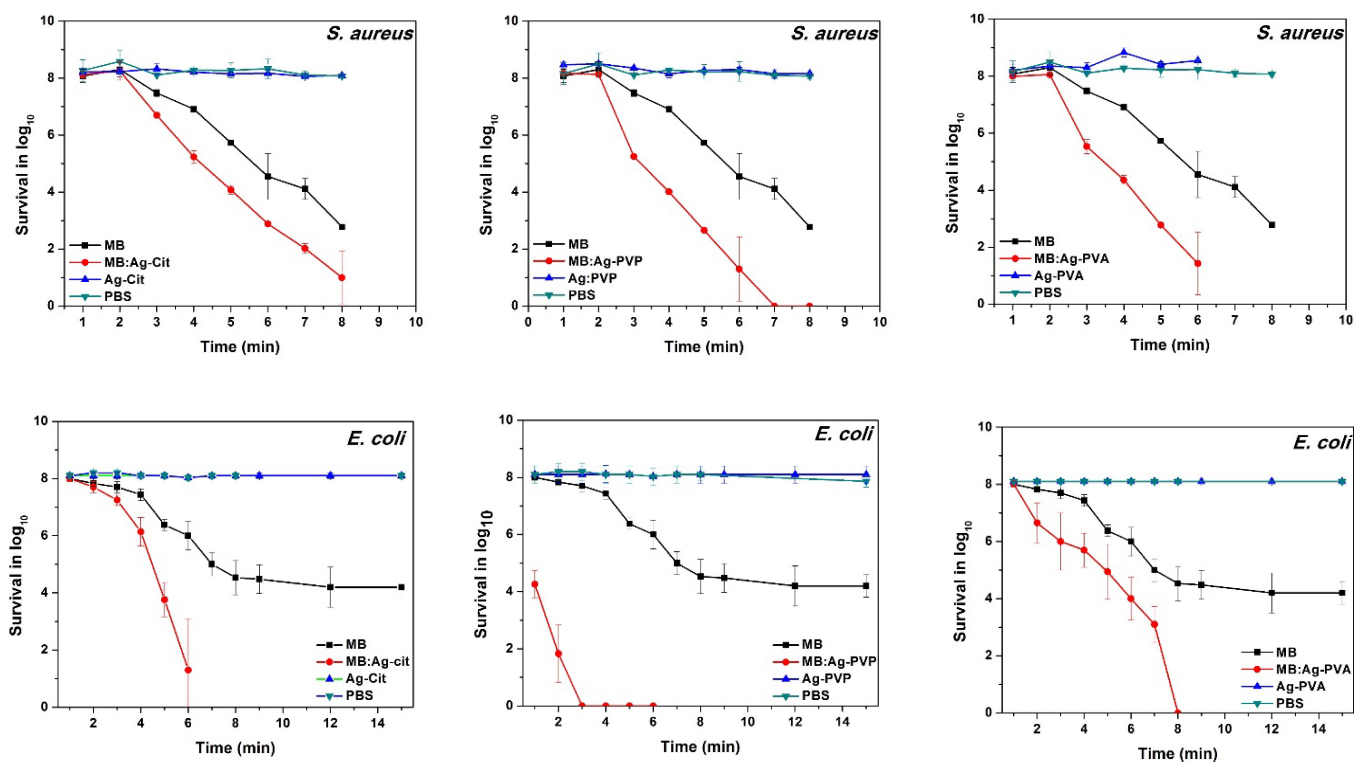


Figure 12 Deactivation of *S. aureus* (upper panels) and *E. coli* (lower panels) bacteria as a function of time in Citrate, PVP, and PVA.

PVA medium. Similarly, MB/Ag NPs deactivated completely 10^8 CFU/ml of *S. aureus* in 8 min in citrate, 7 min in PVP, and 6 min in PVA medium.

Ag NPs synthesized in PVP had most potent antimicrobial activity. While, one minute, irradiation of *E. coli* with MB did not reduce the survival of *E. coli*, MB combined with Ag NPs in PVP decreased the number of bacteria by log of 4 indicating that only 0.01% of bacteria survived the treatment. The similar reduction of *E. coli* with MB alone took 8 min. MB alone could not deactivate *E. coli* completely even after 15 min. Similarly, Ag NPs in citrate medium with MB showed synergistic effect. As shown in Fig. 12, five minutes of irradiation reduced *E. coli* counts by log of 4, while MB alone in 5 min reduced the survival of *E. coli* by log of 2. A similar trend was observed from the results in Fig. 12 with *S. aureus* bacteria. MB coupled with Ag NPs synthesized in different media synergistically showed higher reduction within a shorter period and 99.9% of *S. aureus* is killed with 6-8 min.

Our results show that MB/Ag NPs are more effective in bacterial deactivation. This is mainly due to higher amount of singlet oxygen generation. The singlet oxygen generation efficiency was improved when heavy atoms were used [72]. Enhanced singlet oxygen generation efficiency in the nanoparticles was attributed to efficient intraparticle energy transfer in photosensitizer-doped conjugated polymer nanoparticles [73]. It is known that the efficiency of singlet oxygen generation is proportional to the population of the excited triplet photosensitizers, which are produced by intersystem crossing (ISC) from the excited singlet photosensitizers. Therefore, the Ag NPs probably increase the lifetime of the triplet state of MB and increase the efficiency of ISC from singlet-MB to triplet-MB. In addition to inherent dark toxicity, MB have poor cell/tissue penetration, accumulation, and low biological stability in free molecular form as

they are rapidly reduced to an inactive form, leuco-MB. Thus, the use of MB *in vivo* PDT with cancer was limited due to these limitations.

We have previously reported the influence of size of MB/Ag NPs on inhibition of bacteria. We observed similar effect in this study. Our results suggest that as the size of Ag NPs decreases it becomes more toxic toward both Gram-negative and Gram-positive bacteria [14], probably due to higher probabilities of small Ag NPs to penetrate into bacteria, and damage DNA and mitochondria [74, 75]. Moreover, increase in the surface area-to-volume ratio when particle size decreases lead to higher accumulation of Ag NPs to the bacterial surface; blocking the respiratory system and making it more toxic especially for an aerobic bacterium [76, 77].

In addition, the higher antimicrobial activity of MB/Ag NPs in PVP medium than PVA and citrate might be due to higher release of silver ions (Ag^+) in water. Ag^+ interacts with a number of electron donor functional group such as thiols, phosphates, hydroxyls, imidazole, and indoles [29]. Moreover, developed electrostatic force between negatively charged bacterial cells and positively charged nanoparticles promotes higher interaction between the two entities [60, 61].

3.5. Bacterial uptake

We examined the morphological changes in bacterial cell when irradiated with Ag NPs and its combination with MB using TEM as shown in Fig. 13. It is clearly seen that Ag NPs

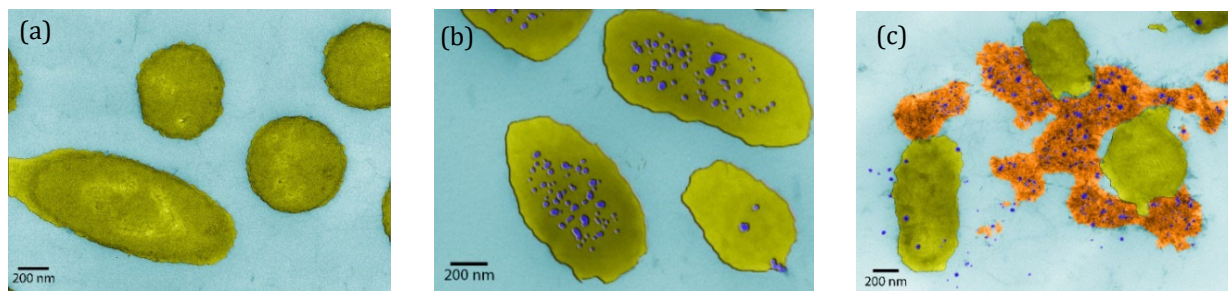


Figure 13 *E. coli* (a) before any treatment, (b) after 6 min of irradiation with Ag NPs and (c) Ag NPs+ MB.

alone do not change the bacteria structure (Fig. 13b) while Ag NPs/MB causes the disruption of the bacterial cell and results in intracellular leakage into environment (Fig. 13c).

3.6. In Vitro cytotoxicity measurements

Although, Ag NPs exhibit antimicrobial activities, their cytotoxicity for adverse health effect due to prolonged exposure at different concentration remains a concern [78-81]. The effects of silver nanoparticles depend on size, surface chemistry, exposure time, concentration, and method of exposure [81-83]. Liver, spleen, lungs, and kidneys are the major target organ for Ag NPs. Nanoparticles are eventually degraded and removed by body, but they are highly stable *in vivo* and have been shown to stay in the blood up to 100 days [82, 84]. Ag NPs were reported to have specific effects in the cells, specifically against protein and DNA. Once internalized, Ag NPs show series of effects such as ROS production, cell cycle arrest, damaging cell membrane, and apoptosis [85, 86]. For instance, it was shown that mitochondrial dysfunction, induction of

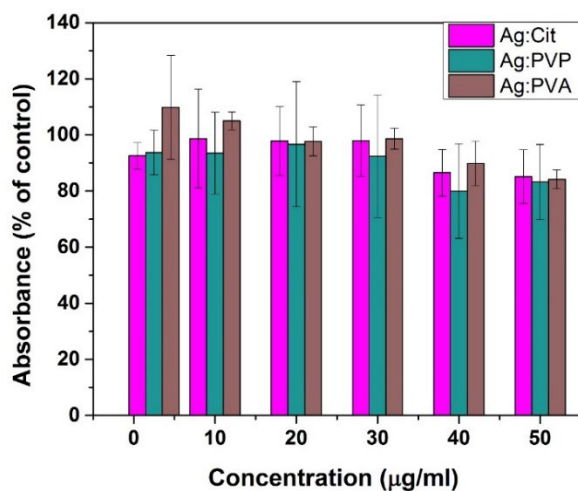


Figure 14 Cytotoxicity measurement of Ag NPS in HEK 293T Cell lines obtained from the American Type Culture Collection was grown in DMEM medium with 10% FBS.

reactive oxygen species by Ag NPs results DNA damage and chromosomal aberrations [87].

According to the published data, the PC12 cells that were treated with 15 nm NPs at a concentration of 10 mg/mL for 24 h induced ROS production and enzymatic dysfunction that

play a crucial role in the depletion of dopamine [88]. In this study, we examined the toxicity of the Ag NPs in a concentration dependent manner for each solution we synthesized and used for antimicrobial analysis. As shown in the Fig. 14, cells cultured with Ag NPs in different solutions grew similar to the PBS treated control cells and show similar viability rate under same growth conditions. In some measurement, an increased cell viability was observed. This could be attributed to an interaction between Ag NPs and membrane proteins that modulate and/or activate signal transduction mechanism involved with cell proliferation and migration. Ag NPs in this study have a minimum average size of 6 nm. Thus, our results shows that Ag NPs do not exhibit cellular cytotoxicity up to a tested level of 50 µg/ml in each solution.

CONCLUSION

The average size of Ag NPs synthesized by using 1064 nm and 532 nm wavelength was found as follows: in citrate 6 and 4 nm; in PVP 10 and 7 nm; in PVA 12 and 10 nm by PLAL method. Material characterizations of Ag NPs were performed by UV–Vis, PL spectroscopy, while the size distribution and the shape of Ag NPs were studied with TEM images. MB/Ag NPs combination showed higher antimicrobial effects compared to MB and Ag NPs alone. Within 6 min of irradiation time with 660 nm LED, the MB/Ag NPs deactivated entire $\sim 10^8$ CFU/mL of Gram-positive, *S. aureus*, and Gram-negative, *E. coli*, bacteria. In addition, bacterial uptake of Ag NPs and morphological changes of bacteria cell were evaluated after PDT experiment. We observed that in agreement with published studies, *E. coli* was more resistant than *S. aureus* to MB treatment. For instance, after 8 min of photodynamic treatment with MB, the number of *E. coli* reduced from log of 8 to log of 4 while *S. aureus* reduced from log of 8 to log of 3. However, when both bacteria were treated with MB/Ag NPs mixture, the *S. aureus* was slightly more resistant. This could be due to difference between intrinsic properties of the bacteria such

as shape (rod vs coccus) or charge on the bacterial surface that could affect the distribution of the MB/Ag NP mixture and thus ROS across the cell surface or it could be due to an extrinsic property of the synthesis medium such as increase in lipophilicity due to hydrocarbon side chains or groups present on PVP, PVA and citrate [89]. This may also be attributing to higher antimicrobial activity of Ag NPs synthesized in PVP in combination with MB. The toxicity of the silver nanoparticles was examined in HEK 293T cell lines obtained from American type culture collection. Our results show that Ag NPs do not exhibit cytotoxicity up to 50 µg/ml in each medium. MB/Ag NPs used in PDT could be effective in killing bacterial pathogens in open wounds, prosthetic joint infections, in vivo cancer, and tumor treatments. In future, we will use MB/Ag NPs combination in synovial fluid obtained from multiple patients to evaluate its effectiveness against pathogens that causes prosthetic joint infection.

APPENDIX A: SAMPLE PREPARATION

1. Phosphate buffer solution preparation with a pH of 7.4.

0.2108 g of potassium phosphate monobasic ($\geq 99.0\%$, Sigma Aldrich), 0.729 g of sodium phosphate dibasic ($\geq 99.0\%$, Sigma Aldrich), and 9.0054 g of sodium chloride (BioXtra, $\geq 99.5\%$, Sigma Aldrich) are weighed and poured into a 1000 ml volumetric flask. DI water is gradually added by mixing the solution each time and filled up to the mark. The PBS solution is then autoclaved in an autoclave bottle for ~ 60 minutes. (P13 cycle).

2. Preparation of PVP solution.

In this project we used 2 mM of Polyvinylpyrrolidone (PVP) aqueous solution. To get 2 mM solution, weight 2.0 g of PVP (Sigma-Aldrich) with average molecular weight of 10,000 g/mol and put into 200 ml beaker. Next, add 100 ml of DI water and mix the solution using magnetic stir plate and magnetic stir bar. All 100 ml of this solution must be used as an aqueous solution in the laser ablation. NOTE: use DI water that is autoclaved since these NPs will be used for the PDT experiment. The DI water from tap might have some microorganisms and be contaminated.

3. Preparation of Sodium Citrate solution.

We kept the concentrations equal for each media. Therefore, to get 2 mM of solution, weighed 35 mg of Sodium Citrate Dihydrate (Fisher) with molecular weight of 294.10 g/mol and put into 200 ml beaker. Next, add 100 ml of DI water and mix the solution well. All 100 ml of this solution must be used as an aqueous solution in the laser ablation. Similarly Polyvinyl alcohol (PVA) solution with 2 mM concentration was prepared.

4. Measurement of Ag NPs concentration in aqueous solution.

To find the mass concentration of Ag NPs, UV-Vis technique was used. Commercially purchased Ag NPs in citrate medium with average size of 10 nm and concentration of 20 µg/ml was used as a known concentration. A linear equation was produced using different diluted concentrations of commercial Ag NPs and that equation was used to find the concentration of synthesized Ag NPs.

5. Methylene blue (6.1×10^{-5} M) preparation.

114 mg of crystalline methylene blue ($\text{MB} \cdot 3\text{H}_2\text{O}$, MW = 373.90 g/mol) is weighed on an electronic scale in biotechnology center (0.1mg sensitivity) and put in a 50 ml sterile centrifuge tube. Clean autoclaved DI water is added and filled up to the mark, the concentration would be 6.1×10^{-4} M. Next, dilution of 10 times was done to get 6.1×10^{-5} M, taking 5 ml from stock solution and adding 45 ml of autoclaved DI water. NOTE: methylene blue should not be autoclaved!

6. LB agar media preparation.

20 g of Luria-Bertani (LB) agar powder (Miller, Difco TM) is weighed and added to a 1 L Erlenmeyer flask filled with 0.25 L of DI water. A magnetic stirring bar is put and mixed until all the powder is dissolved. Then, 0.25 L of DI water is added to remove all the powder that has stuck to the walls of the flask. The flask is covered with an aluminum foil, and an autoclave tape is attached on the top of the flask. Then, the flask is placed in the autoclave (Caution: autoclave gloves must be used) and autoclaved for 60 minutes (Cycle P13). Immediately after the autoclave finishes, the flask is taken out (Caution: autoclave gloves must be used) and let to cool down for no longer than 15 minutes. Then, the LB agar is poured into the sterile Petri plates (single use). Then, the plates are left to cool down for 15 minutes, Fig. A1. When the media has adequately solidified, the plates are turned upside down to prevent condensation of water vapors



Figure A1. Fresh prepared LB agar plates left to solidify.

onto the media and, left in the safety cabinet for about 1-2 hours to dry. After they have dried, the plates are collected, stacked upside down, put in a plastic bag, covered with a tape, and put in a refrigerator to store for later use.

7. LB broth media preparation.

10 g of Luria-Bertani (LB) broth powder (Lennox, Fisher scientific) is weighed out and added to a 1 L Erlenmeyer flask filled with 0.25 L of DI water. A magnetic stirring bar is put and mixed until all the powder is dissolved. Then, 0.25 L of DI water is added to remove all the powder that has stuck to the walls of the flask. The flask is covered with an aluminum foil, and an autoclave tape is attached on the top of the flask. Then, the flask is autoclaved with two more empty glass bottles of 500 ml and 150 ml for 60 minutes (Cycle P13). After the autoclave, the mixture is let to cool down and poured into clean autoclaved bottles and stored for future use, not necessarily in the fridge. Note: if at any time contamination is noticed within the LB broth it should not be used and must be autoclaved before draining down to the sink.

8. Bacterial cell growth on LB broth media.

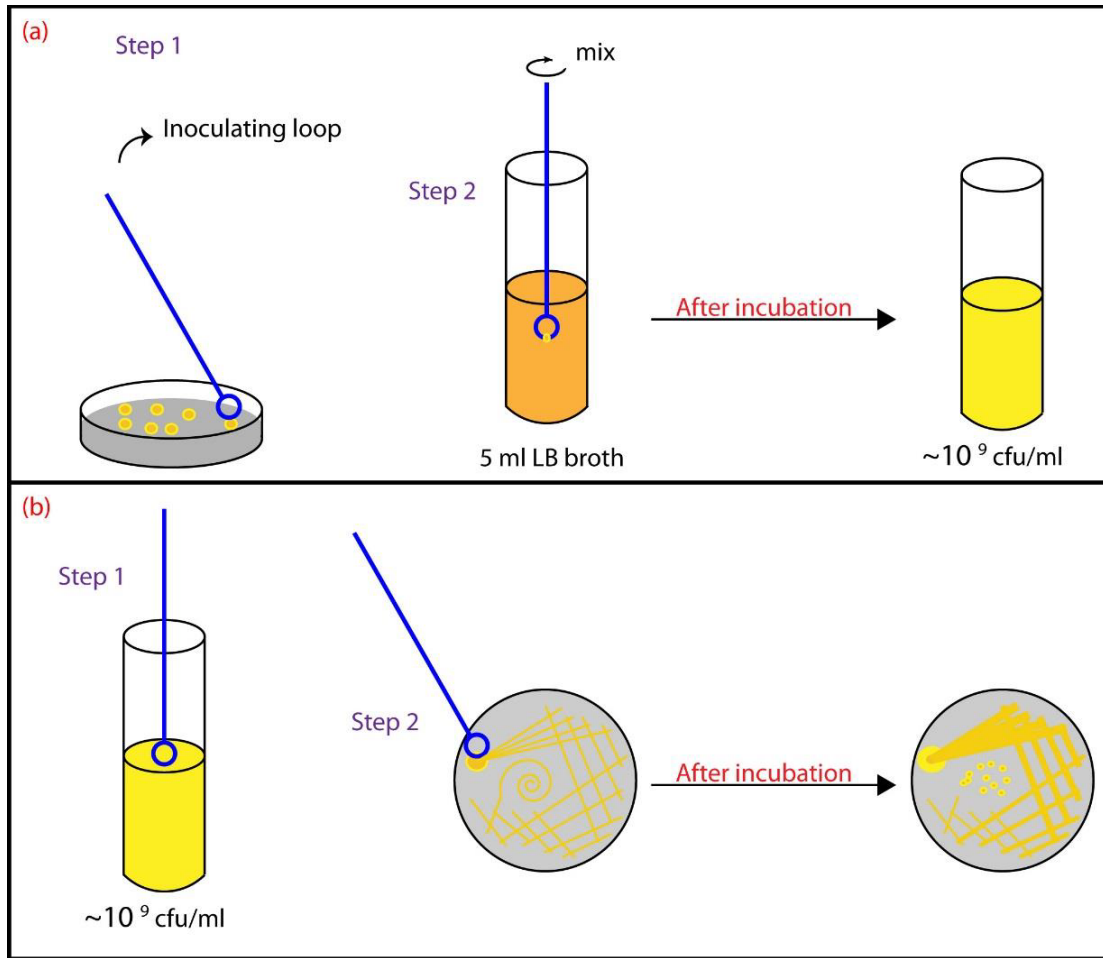


Figure A2. Bacterial cell growth (a) in LB broth media by inoculation (b) and on LB agar media.

Bacteria cells were received on an LB agar media plate in single colonies. Safety cabinet is sterilized by spraying with ethanol (70%) and wiped with a paper towel. A sterile inoculating loop, 14 ml round-bottom tube (Falcon), and 10 ml serological pipette is wiped with ethanol and put under the safety cabinet. Next, the cover of LB broth media is taken and held on the fire

(from Bunsen burner) to keep it sterile. By using the serological pipette, 5 ml of LB broth poured into the round-bottom tube. The inoculating loop is barely touched (for *E. coli*; in case of *S. aureus* the whole colony is taken) on one of the single colonies of bacteria and mixed with LB broth media. The tube is not entirely closed (Oxygen is needed for aerobic bacteria growth) and

incubated at 37 °C and 200 revolutions per minute (RPM) speed for 24 hours approximately.
(Figure A2a)

9. Bacterial cell growth on LB agar media.

Fresh bacteria cells need to be prepared at least every two weeks. After the growth of bacteria in LB broth for 24 hours, an inoculating loop is inserted into the media and then gently touched to the corner of the LB agar plate. From that spot, four lines are drawn without disturbing the media. Each line is separate from one another, and another four lines are drawn from previous lines. This process is repeated two more times, and the plate is flipped upside down put in a plastic zip bag (the bag is left open for air) and incubated at 37 °C for 24 hours approximately. (Figure A2b)

10. Bacteria irradiation procedure.

As it is demonstrated in the Fig. A3, when the bacteria have grown for 24 hours it reaches a concentration of $\sim 10^9$ CFU/ml or more. 3 ml of bacteria is put in cuvette and put in spectrophotometer to measure optical density, if the O. D. for *E. coli* bacteria is equal to $\sim 1.7 \pm 0.5$ then the concentration of bacteria is 10^9 CFU/ml. If the O. D. is much larger it will be diluted to get the above-mentioned concentration using molarity equation which is $= \frac{n(\text{mol})}{V(\text{l})}$. Once the concentration is set to 10^9 CFU/ml we take 100 μL of bacteria for the experiment as shown in the figure A3 below. For *S. aureus* the O. D. should be $\sim 1.4 \pm 0.5$ because it has spherical shape and smaller size than *E. coli* which has rod shape and larger size. The total volume in each well is 1000 μL for all the sample which means it is filled with PBS solution. For instance, 50 μL of MB with concentration of $6.1 * 10^{-5}$ M, 500 μL of Ag NPs solution (from 26 $\mu\text{g}/\text{ml}$ stock solution), 350 μL of PBS, and 100 μL of *E. coli* with O. D. of ~ 1.70 , are mixed in dark for ~ 10 min.

(Longtime vortex mixing should be avoided since it can decrease the number of viable cells due to stress. Speed 10 is okay to use.)

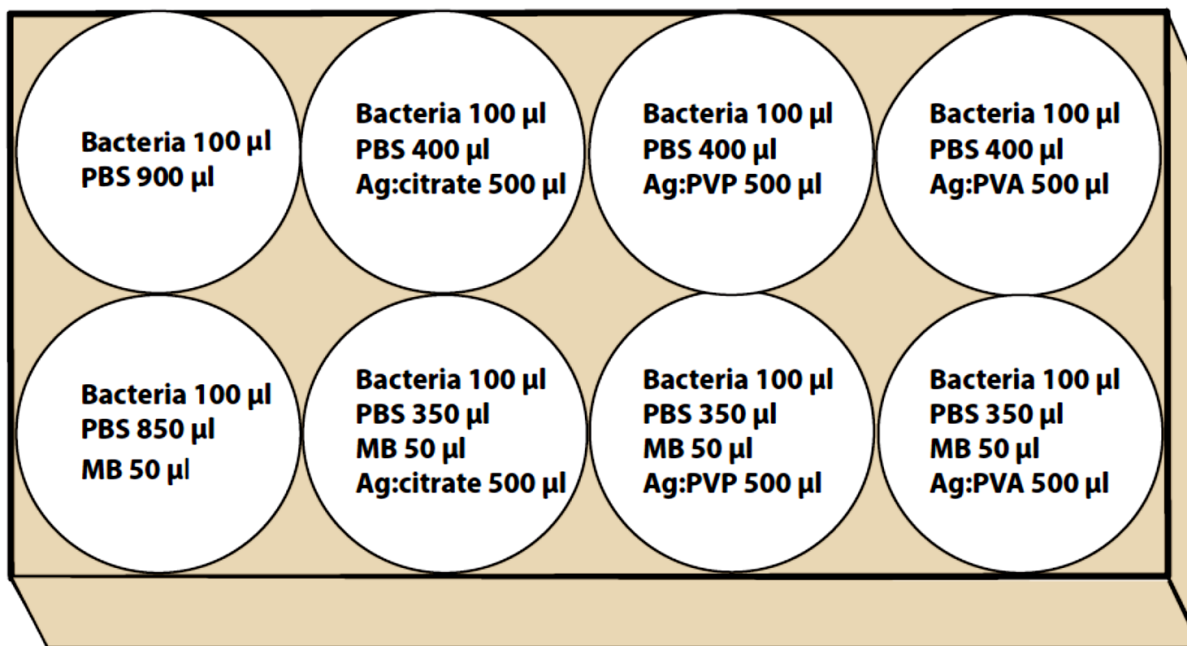


Figure A3. Schematic representation of serial dilution and plating.

In this final mixture, the total volume is 1000 μ L, bacteria have a final concentration of $\sim 10^8$ CFU/ml, and Ag NPs has a concentration of 13 μ g/ml. MB is 6.1×10^{-6} M. Then, the mixture is irradiated for 5 min with a 660 nm LED red light (12 W, from 9 cm), serially diluted, and 50 μ L is poured on LB agar plate, Fig. A4. A cell spreader is immersed in absolute

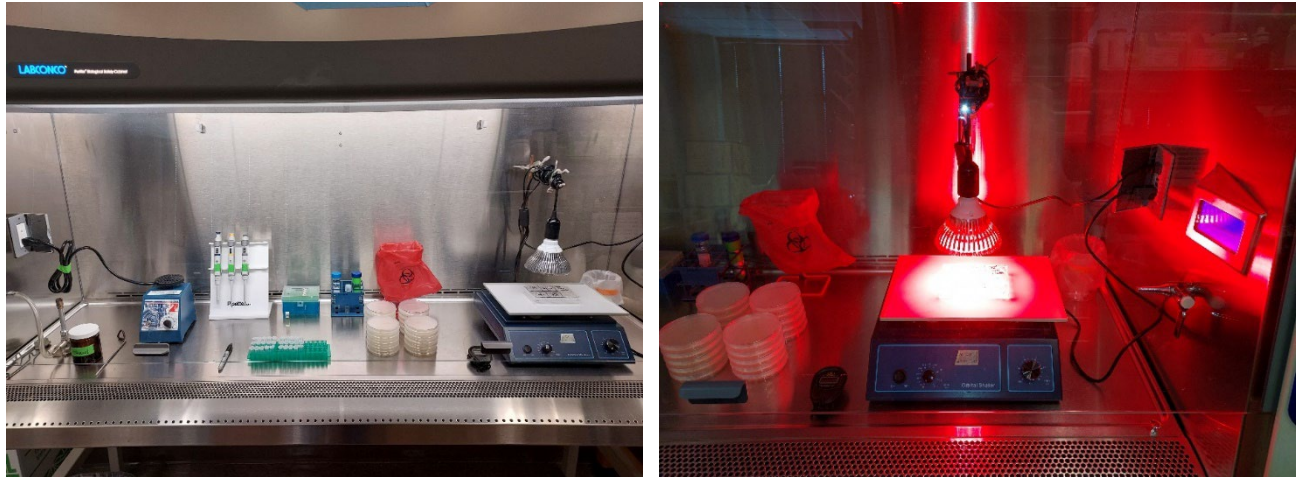


Figure A4. Safety cabinet with the irradiation setup and materials.

ethanol and held over the flame to sterilize it and used to spread the 50 μ L solution on the media gently without disturbing it. Then, the plates are left for the solution to be adsorbed on the media for 10 min and turned upside down, put in a plastic zip bag, and incubated for 24 to 48 hours.

After the incubation, plates are taken out, and the number of colonies is counted visually by marking with a sharpie. The acceptable number of colonies are in the range of 20 – 300 per plate, Fig. A5.

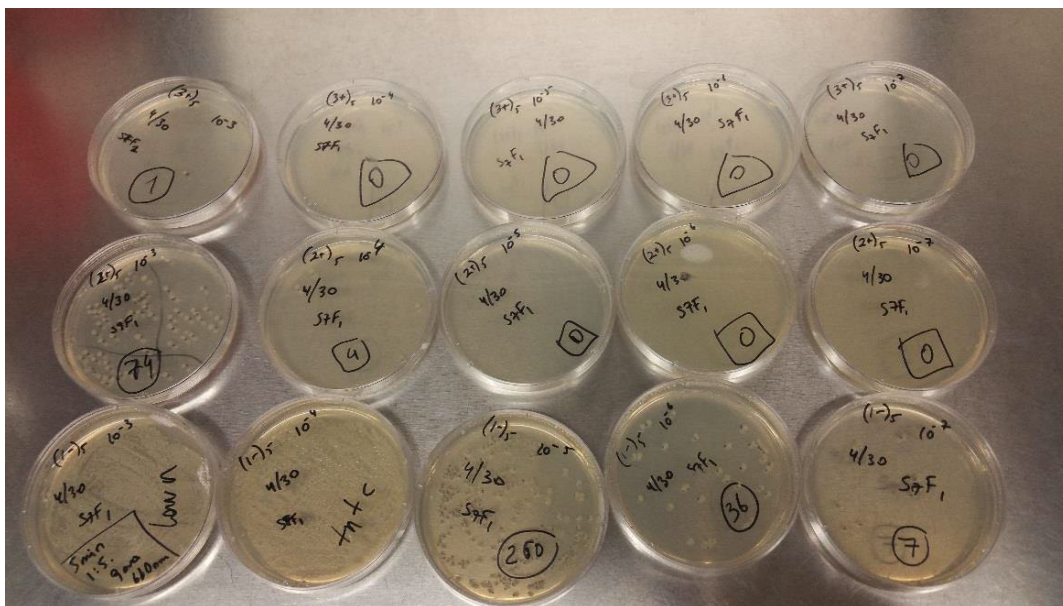


Figure A5. A sample of counted colonies of *E. coli*.

11. Calculation of the number of colony forming units.

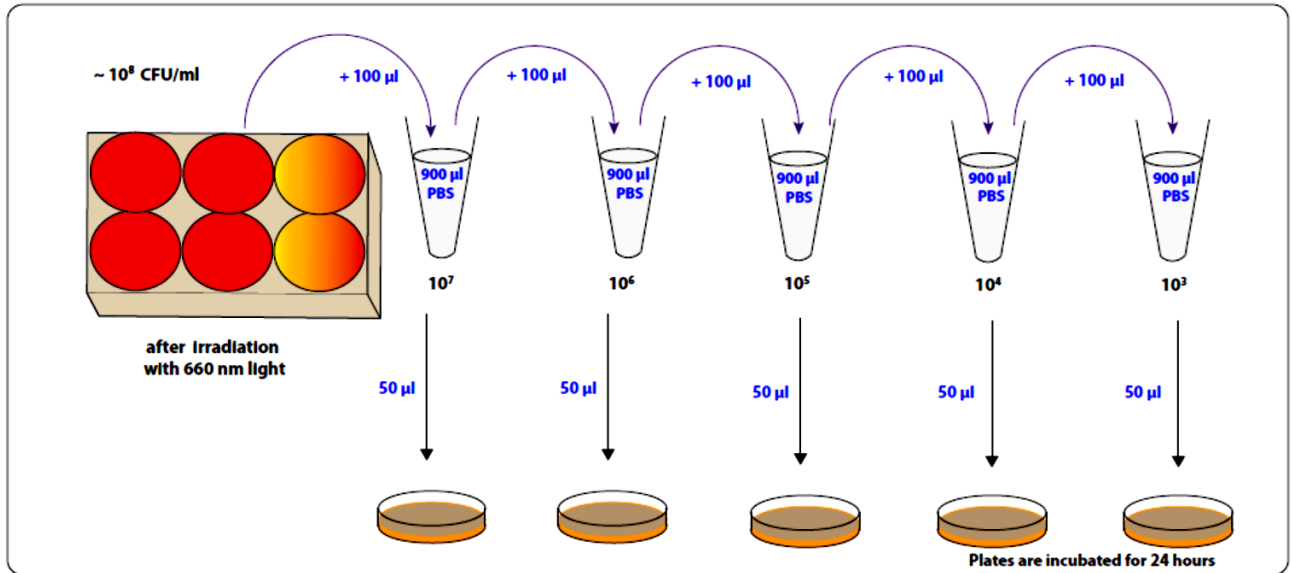


Figure A6. Serial dilution and spread plating of bacteria for counting the number of CFU/ml.

To calculate the concentration of the initial bacteria solution after the incubation, firstly, it is serially diluted, plated on agar media plates, and incubated again for 24 to 48 hours, as shown in Fig. A6. Then, after 24-48 hours the number of the colony forming units are counted, Fig. A7. Plates labeled as “lawn” are the ones that cannot be counted.

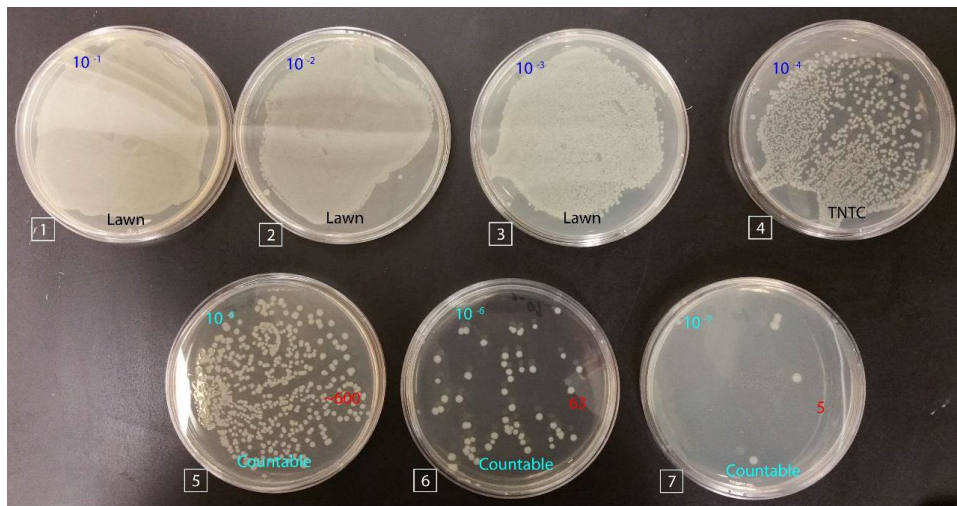


Figure A7. A sample of counted colonies of *E. coli*.

Plates labeled as “TNTC” stands for too numerous to count. So, the only countable plates are mostly 5, 6, and 7. However, the only acceptable ones are plates 5 and 6, if the number of colonies is in the range of 20-300. For instance, for plate 6 the number of colonies is 63. To find the initial concentration of bacteria, the following equation is used:

$$\#CFU = \# \text{ of colonies} \times \text{dilution factor}$$

For example, to find #CFU for plate 6 would be

$$\#CFU = 63 \times 1,000,000 = 63,000,000$$

To find the number of CFU/ml it is multiplied by 1000 and divided by 50 since 50 μ L was pipetted out of 1000 μ L.

$$\#CFU = 63,000,000 \times 20 = 1,260,000,000$$

So, the initial concentration would be 1.26×10^9 CFU/ml.

After 5 minutes of irradiation	CFU/ml	log	After 5 minutes of irradiation	CFU/ml	log
S. aureus control	1.40×10^8	8.15	E. coli	1.80×10^8	8.25
Ag NPs in citrate	1.42×10^8	8.15	Ag NPs in citrate	1.26×10^8	8.10
MB	5.39×10^5	5.73	MB	9.40×10^5	5.97
MB:Ag NPs in citrate	1.24×10^4	4.09	MB:Ag NPs in citrate	5.80×10^3	3.76

Table 1A. Bacteria deactivation results

12. Grid preparation for TEM measurement.

A filter paper (Whatman) is put in a Petri dish and copper grids are put on the filter paper. Copper grids (SPI, 300 mesh, 3 mm) are washed firstly in a hydrochloric acid solution and immediately with DI water to rinse the acid off. Then, they are washed in acetone. A microscope slide (Fisherbrand, Plain precleaned) is taken and soaked inalconox solution (2.5 % w/v) for ~3

min. In the meantime, the column is washed with a “wash” solution (ethylene dichloride) and filled with “Gold” solution (1% formvar in 1,2 dichloroethylene) up to the mark. The microscope slide is taken out and gently dried with a paper towel and with a tissue paper after breathing on it. Then, the slide is slowly inserted vertically into the column and left in the solution for ~ 3 min. The solution is let go and when it reaches the bottom of the column the slide is taken out and put

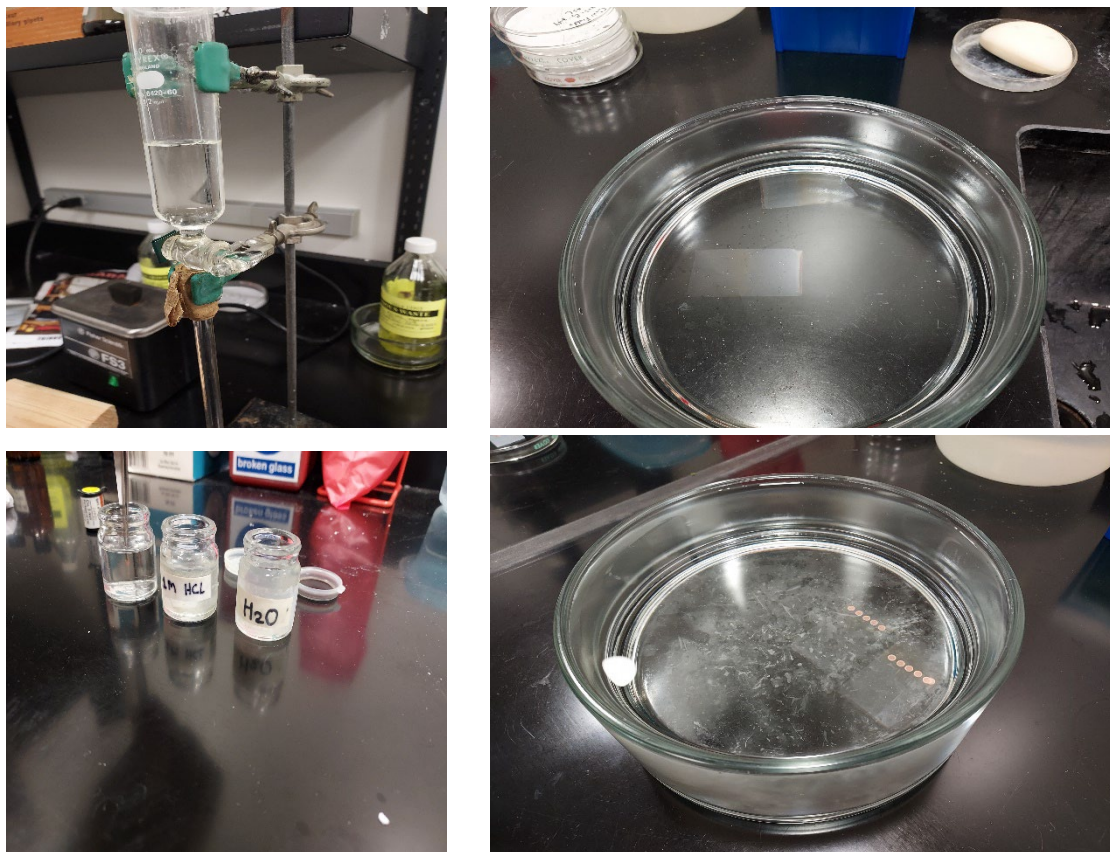


Figure A8. TEM grids on a formvar on DI water.

in a bottle to dry. (If the thicker layer is wanted on the grid the solution should be run faster) After its dry, the edges are scratched with a razor three time. Then, after breathing on the slide it is vertically immersed in a DI water where the two layers come off and the slide is taken out. The grids are put on the layers (where the color is goldish) bright side down, Fig. A8. A piece of parafilm is used to immerse into the water beside the formvar at an angle so that when it starts

going into the water, the formvar sticks to the parafilm. Then, they are both immersed further until all of the formvar is attached to the parafilm and they are pulled back out of the water. The formvar is dried with a filter paper and using a tweezer a circle is drawn around each grid to cut the formvar around them. Then, the grids are gently taken and put in the Petri dish.

Instrument/Material	Company name	Model/purity
Silver target	Sigma-Aldrich	Foil; 1 mm; 99.99%
Methylene blue	Sigma-Aldrich	M9140-25G
ABMDMA	Sigma-Aldrich	75068-50MG
LB agar powder	Fisher Scientific	
LB broth powder	Fisher Scientific	Lennox
Potassium phosphate monobasic	Sigma-Aldrich	≥ 99.0%
Sodium phosphate dibasic	Sigma-Aldrich	≥ 99.0%
Sodium chloride	BioXtra	≥ 99.5%
Sodium citrate dihydrate	Fisher Scientific	BP327-500
Polyvinylpyrrolidone	Sigma-Aldrich	PVP10-500G
Tissue culture plates	Celltreat Scientific Products	6 well
Serological pipet	Celltreat Scientific Products	229010B
Culture tube	Fisher Scientific	
Petri dishes	Fisher Scientific	
Micro centrifuge tubes	Celltreat Scientific Products	
300 mesh super grid	2SPI	
TEM	Jeol	JEM-1400 plus
UV-Vis spectrophotometer	Cole Parmer	2800
Spectrofluorometer	Shimadzu	RF-5301
Centrifuge	Midwest Scientific	
Magnetic stirrer	Sci-Basics	MHS 800

APPENDIX B: Nd: YAG LASER OPERATION

Before turning on the laser, the sign “Laser in use” must be on the door and everyone in the lab should be informed that the laser will be used and that laser safety glasses must be worn all the time while the laser is on.

1. The laser is turned on by turning the key-switch counterclockwise by 90 degrees. The laser should start working, and the “Laser ON” sign turns on as well. The laser should be left on for 5 minutes to warm up before starting the laser.

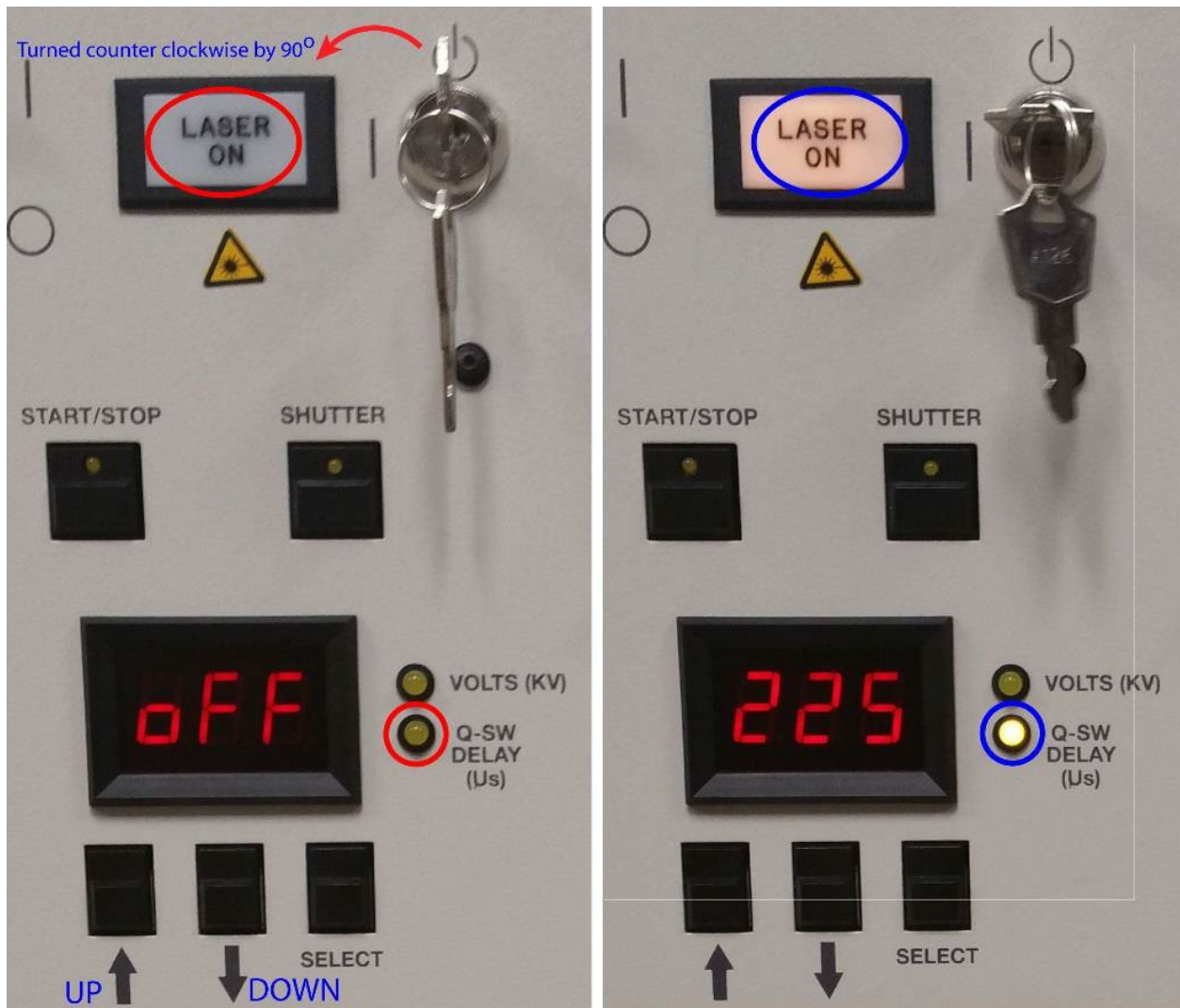


Figure B1. Turning on the laser and changing Q-switch value.

pressed, Fig B2. The laser should start working, a continuous clicking sound will be generated and laser will be working in a continues mode.

5. After letting it run for ~ 5 min, the first shutter is opened by pressing the SHUTTER button (light turns on) and then the second one is opened by sliding to the left, Fig. B3.

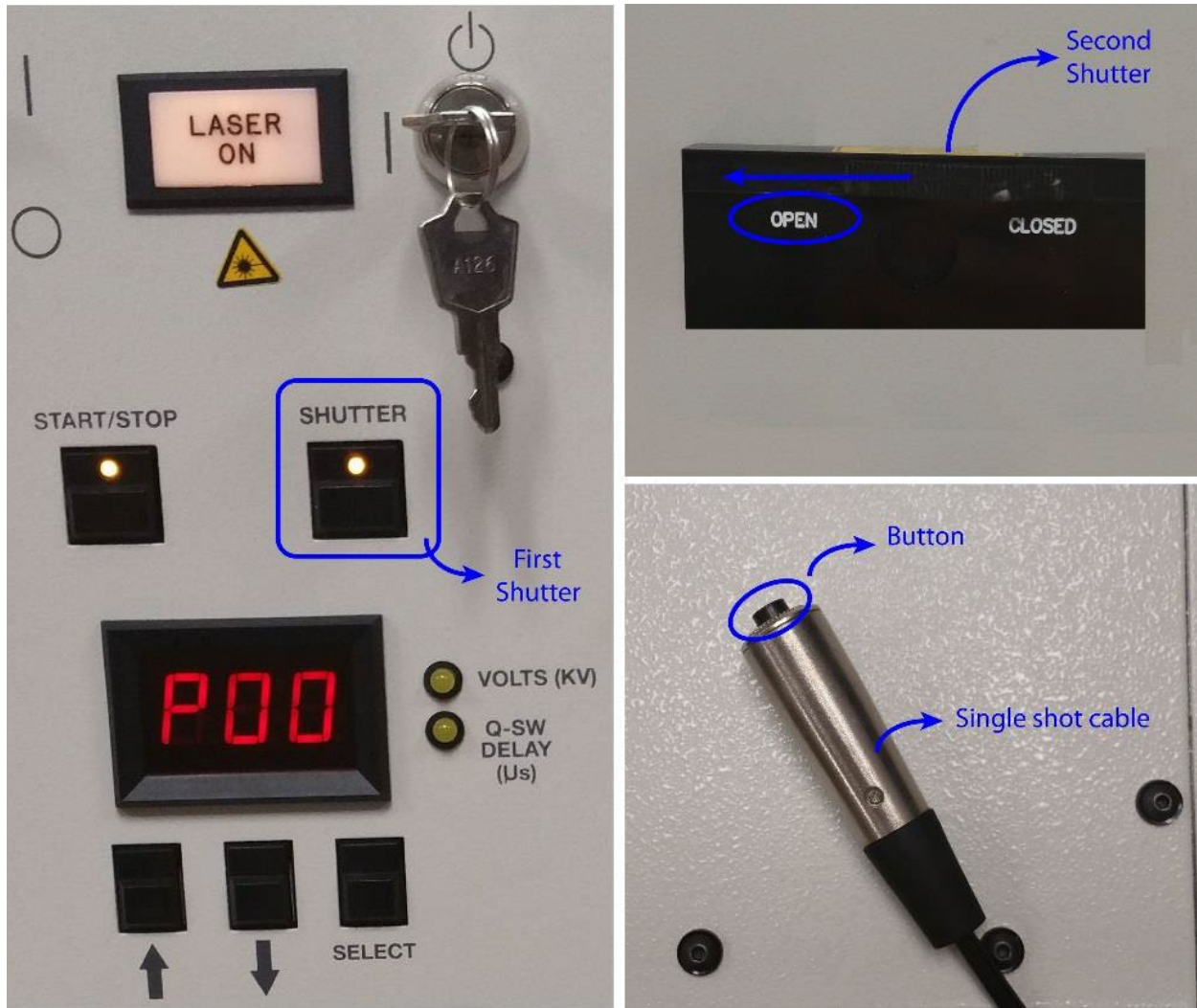


Figure B3. Opening the shutters and the single shot cable.

6. If the Q-switch value needs to be changed during the laser operation, first the shutters

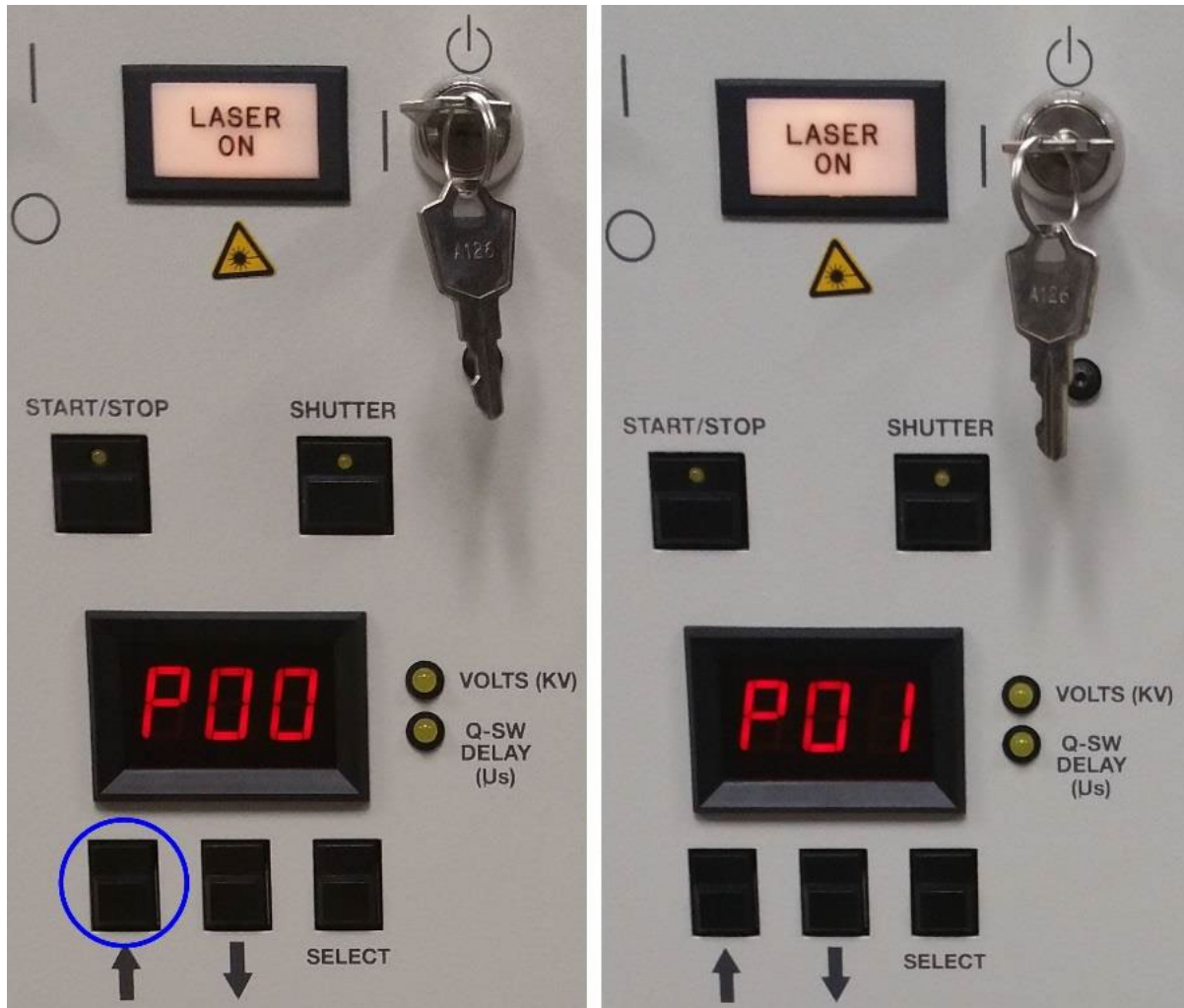


Figure B4. Changing the mode from P00 to P01.

are closed, and the mode is changed from P00 to P01 by using the UP button, Fig. B4. Then, the laser is stopped by pressing START/STOP button, and Q-switch value is changed to the desired value by using UP and DOWN buttons. The mode is changed back to P00 by using the single shot cable, and the laser is started again. Shutters are opened.

7. Once the laser is ON and is ready to operate, the path of the laser beam needs to be checked first to prevent it from hitting a different place other than the surface of a mirror.

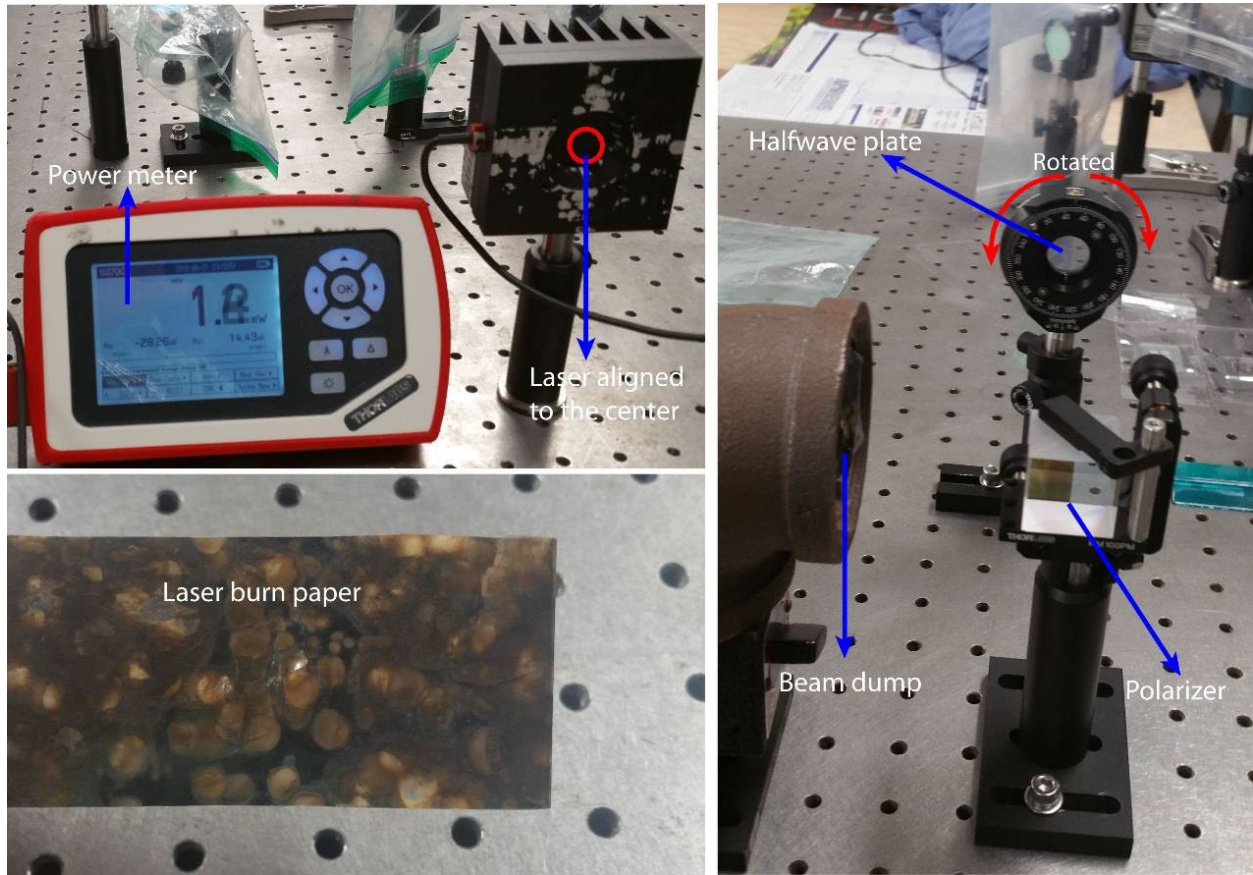


Figure B5. Laser alignment and measuring the power.

This can be done by using a taped “laser burn paper”. If it is not taped first, the dust of the burn paper after laser hit can contaminate the mirror/lense and damage them. When the laser beam is aligned, using a power meter the desired power is adjusted using the polarizer and rotating the halfwave plate. The laser beam passing through the polarizer gets divided into two; one passes through directly and the other reflects at 90-degree angle, so it is important that the latter one is blocked by a beam dump. The laser must hit the center of the power meter and continuous beam should be used by pressing the single shot button and holding it for 5 sec. Then, it is stopped by pressing the single shot cable once, Fig. B5.

8. After the experiment, the power is measured again to verify that it has not changed. Then, the shutters are closed, and mode is changed from P00 to P01 using the UP button. The laser is stopped pressing the START/STOP button and after few minutes the key is turned clockwise to switch the laser off.

References

1. <https://www.cdc.gov/drugresistance/biggest-threats.html>.
2. S. Reardon, B.a.r.r.u., *Nature* 521, 402-403 (2015).
3. Lucky, S.S., K.C. Soo, and Y. Zhang, *Nanoparticles in Photodynamic Therapy*. Chemical Reviews, 2015. **115**(4): p. 1990-2042.
4. Hamblin, M.R. and T. Hasan, *Photodynamic therapy: a new antimicrobial approach to infectious disease?* Photochem Photobiol Sci, 2004. **3**(5): p. 436-50.
5. Gilaberte, Y., et al., *Editorial: Antimicrobial Photodynamic Therapy: A New Paradigm in the Fight Against Infections*. Frontiers in Medicine, 2021. **8**.
6. M. R. Hamblin, Y.-Y.H., *Handbook of Photomedicine*, Taylor & Francis , New York, NY 2013.
7. M. E. Bulina, D.M.C., O. V. Britanova, Y. G. Yanushevich, D. B. Staroverov, T. V. Chepurnykh, E. M. Merzlyak, M. A. Shkrob, S. Lukyanov, K. A. Lukyanov, *A genetically encoded photosensitizer*, Nat Biotech 24, 95-99 (2006).
8. Wainwright, M., Photodynamic antimicrobial chemotherapy (PACT), *J. Antimicro. Chemo* 42 (1998) 13-28.
9. Zeina, B., et al., *Killing of cutaneous microbial species by photodynamic therapy*. Br J Dermatol, 2001. **144**(2): p. 274-8.
10. Dai, T., Y.-Y. Huang, and M.R. Hamblin, *Photodynamic therapy for localized infections—State of the art*. Photodiagnosis and Photodynamic Therapy, 2009. **6**(3-4): p. 170-188.
11. Ross, W.B., D. Dolphin, Structure and Biodistribution Relationships of Photodynamic Sensitizers, *Photochem. Photobiol.* 64 (1996) 469-485.
12. Müller-Breitkreutz, K., H. Mohr, K. Briviba, H. Sies, Inactivation of viruses by chemically and photochemically generated singlet molecular oxygen, *J. Photochem. Photobio. B* 30 (1995) 63-70.
13. Kholikov, K., Ilhom, S., Sajjad, M., Smith, M. E., Monroe, J. D., San, O., & Er, A. O. , *Improved singlet oxygen generation and antimicrobial activity of sulphur-doped graphene quantum dots coupled with methylene blue for photodynamic therapy applications*. Photodiagnosis and Photodynamic Therapy, 2018. **24**: p. 7–14.
14. Belekov, E., et al., *Improved antimicrobial properties of methylene blue attached to silver nanoparticles*. Photodiagnosis and Photodynamic Therapy, 2020. **32**: p. 102012.
15. Fu, X., Y. Fang, and M. Yao, *Antimicrobial photodynamic therapy for methicillin-resistant Staphylococcus aureus infection*. Biomed Res Int., 2013. **2013**: p. 159157. doi 10.1155/2013/159157. Epub 2013 Feb 28.
16. T. Briggs, et al.
17. Redmond, R.W. and J.N. Gamlin, *A Compilation of Singlet Oxygen Yields from Biologically Relevant Molecules*. Photochemistry and Photobiology, 1999. **70**(4): p. 391-475.
18. Li, R., et al., *Synergistic reaction of silver nitrate, silver nanoparticles, and methylene blue against bacteria*. Proceedings of the National Academy of Sciences, 2016. **113**(48): p. 13612-13617.
19. Wojtoniszak, M., et al., *Graphene oxide functionalized with methylene blue and its performance in singlet oxygen generation*. Materials Research Bulletin, 2013. **48**(7): p. 2636-2639.
20. Er, A.O., et al., *Inactivation of bacteria in plasma*. Photochem Photobiol Sci, 2012. **11**(11): p. 1700-4.
21. Chatterjee, D.K., L.S. Fong, and Y. Zhang, *Nanoparticles in photodynamic therapy: an emerging paradigm*. Adv Drug Deliv Rev, 2008. **60**(15): p. 1627-37.
22. Yoon, H.K., et al., *Polymer-Protein Hydrogel Nanomatrix for Stabilization of Indocyanine Green towards Targeted Fluorescence and Photoacoustic Bio-imaging*. J Mater Chem B, 2013. **1**(41).

23. Lara, H.H., et al., *Silver nanoparticles are broad-spectrum bactericidal and virucidal compounds*. J Nanobiotechnology, 2011. **9**(30): p. 1477-3155.
24. Rai, M., A. Yadav, and A. Gade, *Silver nanoparticles as a new generation of antimicrobials*. Biotechnol Adv, 2009. **27**(1): p. 76-83.
25. Rai, M.K., et al., *Silver nanoparticles: the powerful nanoweapon against multidrug-resistant bacteria*. J Appl Microbiol, 2012. **112**(5): p. 841-52.
26. Dakal, T.C., et al., *Mechanistic Basis of Antimicrobial Actions of Silver Nanoparticles*. Front Microbiol, 2016. **7**(1831).
27. Alexander, J.W., *History of the medical use of silver*. Surg Infect, 2009. **10**(3): p. 289-92.
28. Duran, N., et al., *Silver nanoparticles: A new view on mechanistic aspects on antimicrobial activity*. Nanomedicine, 2016. **12**(3): p. 789-799.
29. Franci, G., et al., *Silver nanoparticles as potential antibacterial agents*. Molecules, 2015. **20**(5): p. 8856-74.
30. Wang, L., C. Hu, and L. Shao, *The antimicrobial activity of nanoparticles: present situation and prospects for the future*. Int J Nanomedicine, 2017. **12**: p. 1227-1249.
31. Helmlinger, J., et al., *Silver nanoparticles with different size and shape: equal cytotoxicity, but different antibacterial effects*. RSC Advances, 2016. **6**(22): p. 18490-18501.
32. Ivask, A., et al., *Size-Dependent Toxicity of Silver Nanoparticles to Bacteria, Yeast, Algae, Crustaceans and Mammalian Cells In Vitro*. PLOS ONE, 2014. **9**(7): p. e102108.
33. Kim, T.H., et al., *Size-dependent cellular toxicity of silver nanoparticles*. J Biomed Mater Res A, 2012. **100**(4): p. 1033-43.
34. Q. H. Tran, V.Q.N., A.-T. Le, *Silver nanoparticles: synthesis, properties, toxicology, applications and perspectives*, Adv. Nat. Sci. 4, 033001 (2013).
35. Au - Ratti, M., et al., *Production of Metal Nanoparticles by Pulsed Laser-ablation in Liquids: A Tool for Studying the Antibacterial Properties of Nanoparticles*. JoVE, 2017(124): p. e55416.
36. Bae, C.H., S.H. Nam, and S.M. Park, *Formation of silver nanoparticles by laser ablation of a silver target in NaCl solution*. Applied Surface Science, 2002. **197-198**: p. 628-634.
37. Tsuji, T., et al., *Preparation of silver nanoparticles by laser ablation in polyvinylpyrrolidone solutions*. Applied Surface Science, 2008. **254**(16): p. 5224-5230.
38. Lam, J., *Pulsed Laser Ablation in Liquid : towards the comprehension of the growth processes Vers la compréhension des processus de croissance en ablation laser en milieu liquide*. 2015, Université Claude Bernard - Lyon I.
39. Eason, R., *Pulsed laser deposition of thin films : applications-led growth of functional materials*. 2007, Hoboken, N.J.: Wiley-Interscience. xxiii, 682 p.
40. Hamad, A.H., et al., *Sequential laser and ultrasonic wave generation of TiO₂@Ag core-shell nanoparticles and their anti-bacterial properties*. Lasers Med Sci, 2016. **31**(2): p. 263-73.
41. Kaselouris, E., et al., *A Review of Simulation Methods of Laser Matter Interactions Focused on Nanosecond Laser Pulsed Systems*. Journal of Multiscale Modelling, 2015. **05**: p. 1330001.
42. Chichkov, B.N., et al., *Femtosecond, picosecond and nanosecond laser ablation of solids*. Applied Physics A, 1996. **63**(2): p. 109-115.
43. Wang, X., D.M. Riffe, Y.-S. Lee and M. Downer, *Time-resolved electron-temperature measurement in a highly excited gold target using femtosecond thermionic emission*. Physical Review B, 1994. **50**(11): p. 8016.
44. Zhang, Z., et al., *First-principles modeling of laser-matter interaction and plasma dynamics in nanosecond pulsed laser shock processing*. Journal of Applied Physics, 2018. **123**(5): p. 054901.
45. Sukhov, I.A., G.A. Shafeev, V.V. Voronov, M. Sygletou, E. Stratakis and C. Fotakis, *Generation of nanoparticles of bronze and brass by laser ablation in liquid*. Applied Surface Science, 2014. **302**: p. 79-82.

46. Yang, G.W., *Laser ablation in liquids: Applications in the synthesis of nanocrystals*. Progress in Materials Science, 2007. **52**(4): p. 648-698.
47. Xiao, J., et al., *External field-assisted laser ablation in liquid: An efficient strategy for nanocrystal synthesis and nanostructure assembly*. Progress in Materials Science, 2017. **87**: p. 140-220.
48. Reich, S., et al., *Fluence Threshold Behaviour on Ablation and Bubble Formation in Pulsed Laser Ablation in Liquids*. Chemphyschem, 2017. **18**(9): p. 1084-1090.
49. Petkovšek, R. and P. Gregorčič, *A laser probe measurement of cavitation bubble dynamics improved by shock wave detection and compared to shadow photography*. Journal of Applied Physics, 2007. **102**(4): p. 044909.
50. Heinz, H., et al., *Nanoparticle decoration with surfactants: Molecular interactions, assembly, and applications*. Surface Science Reports, 2017. **72**(1): p. 1-58.
51. Shrestha, S., B. Wang, and P. Dutta, *Nanoparticle processing: Understanding and controlling aggregation*. Advances in Colloid and Interface Science, 2020. **279**: p. 102162.
52. Norsyuhada, W., et al., *Synthesis and Characterization of Gold-Silver Nanoparticles in Deionized Water by Pulsed Laser Ablation (PLAL) Technique at Different Laser Parameter*. International Journal of Nanoscience, 2019. **18**(01): p. 1850015.
53. Verma, R.K., K. Kumar, and S.B. Rai, *Pulsed laser ablation synthesis of silver nanoparticles and their use in fluorescence enhancement of Tb³⁺-doped aluminosilicate glass*. Solid State Communications, 2010. **150**: p. 1947-1950.
54. Menazea, A.A., *Femtosecond laser ablation-assisted synthesis of silver nanoparticles in organic and inorganic liquids medium and their antibacterial efficiency*. Radiation Physics and Chemistry, 2020. **168**: p. 108616.
55. Tajdidzadeh, M., et al., *Synthesis of silver nanoparticles dispersed in various aqueous media using laser ablation*. TheScientificWorldJournal, 2014. **2014**: p. 324921-324921.
56. Sportelli, M.C., et al., *The Pros and Cons of the Use of Laser Ablation Synthesis for the Production of Silver Nano-Antimicrobials*. Antibiotics (Basel), 2018. **7**(3).
57. Hilal, H., *Re: What is the main reason that nano particles get agglomerated?* Retrieved from: <https://www.researchgate.net/post/What-is-the-main-reason-that-nano-particles-get-agglomerated/53309322d039b184118b4619/citation/download.>, 2014.
58. Al-Nassar, S.I., F.I. Hussein, and A.K. M, *The effect of laser pulse energy on ZnO nanoparticles formation by liquid phase pulsed laser ablation*. Journal of Materials Research and Technology, 2019. **8**(5): p. 4026-4031.
59. Dorrnian, D., Ahmadi Afshar, S.A., Tahmasebi, N. et al. Effect of Laser Pulse Energy on the Characteristics of Cu Nanoparticles Produced by Laser Ablation Method in Acetone. J Clust Sci 25, 1147–1156 (2014). .
60. G. Yang, L.A.i.L.P.a.A.i. and P.S. the Preparation of Nanomaterials, 2012.
61. De Leersnyder, I., et al., *High Variability in Silver Particle Characteristics, Silver Concentrations, and Production Batches of Commercially Available Products Indicates the Need for a More Rigorous Approach*. Nanomaterials, 2020. **10**(7): p. 1394.
62. He, R., et al., *Preparation of polychrome silver nanoparticles in different solvents*. Journal of Materials Chemistry, 2002. **12**(12): p. 3783-3786.
63. G. Mie Ann. Phys., 25 , 377.
64. Oseguera-Galindo, D.O., et al., *Effects of the confining solvent on the size distribution of silver NPs by laser ablation*. Journal of Nanoparticle Research, 2012. **14**(9): p. 1133.
65. Amendola, V., S. Polizzi, and M. Meneghetti, *Free Silver Nanoparticles Synthesized by Laser Ablation in Organic Solvents and Their Easy Functionalization*. Langmuir, 2007. **23**(12): p. 6766-6770.

66. Alrahili, M., et al., *Absorption cross section of gold nanoparticles based on NIR laser heating and thermodynamic calculations*. Scientific Reports, 2020. **10**(1): p. 18790.
67. Vijayakumar, R., et al., *Green synthesis and characterization of gold nanoparticles using extract of anti-tumor potent Crocus sativus*. Physica E: Low-dimensional Systems and Nanostructures, 2011. **44**(3): p. 665-671.
68. Singh, S., et al., *Traumatic Incidents and Experiences of Racism and Sexism: Examining Associations with Components of Critical Consciousness for System-Involved Girls of Color*. American Journal of Community Psychology, 2021. **67**(1-2): p. 64-75.
69. Olson, J., et al., *Optical characterization of single plasmonic nanoparticles*. Chemical Society Reviews, 2015. **44**(1): p. 40-57.
70. Smitha, S.L., et al., *Studies on surface plasmon resonance and photoluminescence of silver nanoparticles*. Spectrochimica Acta Part A: Molecular and Biomolecular Spectroscopy, 2008. **71**(1): p. 186-190.
71. Yeshchenko, O.A., et al., *Size-dependent surface-plasmon-enhanced photoluminescence from silver nanoparticles embedded in silica*. Physical Review B, 2009. **79**(23): p. 235438.
72. Shen, X., et al., *Enhanced Two-Photon Singlet Oxygen Generation by Photosensitizer-Doped Conjugated Polymer Nanoparticles*. Langmuir, 2011. **27**(5): p. 1739-1744.
73. Tekade, S.P., et al., *Hydrogen generation through water splitting reaction using waste aluminum in presence of gallium*. International Journal of Hydrogen Energy, 2020. **45**(44): p. 23954-23965.
74. Wu, D., et al., *Evaluation of the antibacterial efficacy of silver nanoparticles against Enterococcus faecalis biofilm*. J Endod, 2014. **40**(2): p. 285-90.
75. Tamayo, L.A., et al., *Release of silver and copper nanoparticles from polyethylene nanocomposites and their penetration into Listeria monocytogenes*. Mater Sci Eng C Mater Biol Appl, 2014. **40**: p. 24-31.
76. Matsumura, Y., et al., *Mode of bactericidal action of silver zeolite and its comparison with that of silver nitrate*. Appl Environ Microbiol, 2003. **69**(7): p. 4278-81.
77. Shrivastava, S., et al., *Characterization of enhanced antibacterial effects of novel silver nanoparticles*. Nanotechnology, 2007. **18**(22): p. 225103.
78. Liao, C., Y. Li, and S.C. Tjong, *Bactericidal and Cytotoxic Properties of Silver Nanoparticles*. International journal of molecular sciences, 2019. **20**(2): p. 449.
79. Arora S, J.J., Rajwade JM, Paknikar KM. Cellular responses induced by silver nanoparticles: In vitro studies. Toxicol Lett 2008;179:93–100.
80. Ahamed M, A.M., Siddiqui MK. Silver nanoparticle applications and human health. Clin Chim Acta 2010;411:1841–1848.
81. Zhang, T., et al., *Cytotoxic Potential of Silver Nanoparticles*. Yonsei Med J, 2014. **55**(2): p. 283-291.
82. Lankveld DP, O.A., Krystek P, Neigh A, Troost-de Jong A, Noorlander CW, et al. The kinetics of the tissue distribution of silver nanoparticles of different sizes. Biomaterials 2010;31:8350–8361.
83. Gliga, A.R., et al., *Size-dependent cytotoxicity of silver nanoparticles in human lung cells: the role of cellular uptake, agglomeration and Ag release*. Particle and Fibre Toxicology, 2014. **11**(1): p. 11.
84. Ballou B, E.L., Andreko S, Harper T, Fitzpatrick JA, Waggoner AS, Bruchez MP. Sentinel lymph node imaging using quantum dots in mouse tumor models. Bioconjug Chem. 2007 Mar-Apr;18:389–96.
85. Singh RP, R.P.C.u., intracellular trafficking and cytotoxicity of silver nanoparticles. Toxicol Lett 2012;213:249–259.

86. Almofti MR, I.T., Yamashita K, Terada H, Shinohara Y. Silver ion induces a cyclosporine a-insensitive permeability transition in rat liver mitochondria and release of apoptogenic cytochrome C. *J Biochem* 2003;134:43–49.
87. P. Asharani, C.a.g.o.s.n.i.h.c.A. and -. *Nano* 3.
88. Wang, J., et al., *Expression changes of dopaminergic system-related genes in PC12 cells induced by manganese, silver, or copper nanoparticles*. *NeuroToxicology*, 2009. **30**(6): p. 926-933.
89. Banfi, S., et al., *Antibacterial activity of tetraaryl-porphyrin photosensitizers: An in vitro study on Gram negative and Gram positive bacteria*. *Journal of Photochemistry and Photobiology B: Biology*, 2006. **85**(1): p. 28-38.

Copyright Permission

Name: Hakimov, Somon

Email (to receive future readership statistics): somon.hakimov248@topper.wku.edu

Type of document: ['Thesis']

Title: EVALUATION OF SILVER NANOPARTICLES ATTACHED TO METHYLENE BLUE AS AN ANTIMICROBIAL AGENT AND ITS CYTOTOXICITY

Keywords (3-5 keywords not included in the title that uniquely describe content): silver nanoparticles, methylene blue, photodynamic therapy

Committee Chair: Dr. Ali Oguz Er

Additional Committee Members: Dr. Ivan Novikov Dr. Simran Banga

Select 3-5 TopSCHOLAR® disciplines for indexing your research topic in TopSCHOLAR®: Physics, biology, chemistry

Copyright Permission for TopSCHOLAR® (digitalcommons.wku.edu) and ProQuest research repositories:

I hereby warrant that I am the sole copyright owner of the original work.

I also represent that I have obtained permission from third party copyright owners of any material incorporated in part or in whole in the above described material, and I have, as such identified and acknowledged such third-part owned materials clearly. I hereby grant Western Kentucky University the permission to copy, display, perform, distribute for preservation or archiving in any form necessary, this work in TopSCHOLAR® and ProQuest digital repository for worldwide unrestricted access in perpetuity. I hereby affirm that this submission is in compliance with Western Kentucky University policies and the U.S. copyright laws and that the material does not contain any libelous matter, nor does it violate third-party privacy. I also understand that the University retains the right to remove or deny the right to deposit materials in TopSCHOLAR® and/or ProQuest digital repository.

['I grant permission to post my document in TopSCHOLAR and ProQuest for unrestricted access.']

The person whose information is entered above grants their consent to the collection and use of their information consistent with the Privacy Policy. They acknowledge that the use of this service is subject to the Terms and Conditions.

['I consent to the above statement.']